


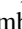









Natural sources of intense ultra-high-frequency radiation in high-voltage atmospheric dischargesE. V. Parkevich ^{1,*}, A. I. Khirianova ¹, T. F. Khirianov ¹, I. S. Baidin ¹, K. V. Shpakov ¹, D. V. Tolbukhin ¹,
A. A. Rodionov ¹, Ya. K. Bolotov ^{1,2}, V. A. Ryabov ¹, S. A. Ambrozevich ³, and A. V. Oginov ¹¹*P. N. Lebedev Physical Institute of the Russian Academy of Sciences, 53 Leninskiy Prospekt, Moscow 119991, Russia*²*Moscow Institute of Physics and Technology, Institutskiy Pereulok 9, Dolgoprudny, Moscow Region 141700, Russia*³*Bauman Moscow State Technical University, 5/1 2-ya Baumanskaya Street, Moscow 105005, Russia*

(Received 22 May 2023; accepted 11 July 2023; published 8 August 2023)

We study the sources of intense ultra-high-frequency (UHF) radiation (in the frequency range 1–6 GHz) arising during the development of high-voltage atmospheric discharges. The discharges were initiated in a long discharge gap by applying an approximately 1-MV pulse with positive or negative polarity. By employing a radio registration system based on ultrawideband antennas, we managed to localize the UHF radiation sources in the discharge with centimeter accuracy and investigate their temporal and spatial correlation with the discharge structures. The vast majority of the localized sources turned out to be concentrated in the near-electrode regions. It is found that the generation mechanism of intense UHF radiation in a laboratory discharge cannot be unambiguously associated with such basic processes as the head-on collision of opposite-polarity streamers or the interaction of single streamers with the near-electrode plasma at the surface of metal electrodes. We discovered that the observed UHF emission appears basically as a precursor of the intense plasma development in a certain discharge region, whereinto a bright counterstreamer comes a bit later. The findings were confirmed by the statistical observations and results of imaging the dynamics of the discharge structures with a nanosecond temporal resolution.

DOI: [10.1103/PhysRevE.108.025201](https://doi.org/10.1103/PhysRevE.108.025201)**I. INTRODUCTION**

According to modern concepts [1], the sources of intense ultra-high-frequency (UHF) radiation (at frequencies above 1 GHz) in extended electrical discharges are related to the space regions wherein the head-on collisions of opposite-polarity streamers occur. It is assumed that the streamer collision process is accompanied by high-frequency oscillations of the current in plasma on timescales shorter than 1 ns [2,3]. Rapid current variations with a high amplitude can cause the UHF emission. This assumption finds theoretical confirmations in numerical studies [4,5], although direct evidences in experiments have not been obtained yet. Apart from the unknown nature of the UHF radiation sources, there is still a significant lack of experimental measurements of such a type of electromagnetic radiation arising during the development of extended high-voltage discharges. Only in recent studies [6–8] were comprehensive data on the temporal and spectral characteristics of the UHF emissions obtained in a wide frequency range (1–10 GHz), and the discharge dynamics was traced during the emergence of such radiation. It was shown that the observed UHF emissions appear as multiple single bursts with a high power and duration shorter than 1 ns, which are characterized by frequencies in the range 1–4 GHz. A particular correlation between the emergences of UHF radiation and hard x rays in the discharge was observed as well [9,10]. Indeed, it was found in [8] that during the

generation of UHF radiation the power of the radio emission in the frequency range 10–150 MHz significantly increases, with the maximum power of such an emission being reached at 65–85 MHz. Based on this fact, one can assume that radio flashes in the megahertz frequency range, which are widely employed in monitoring extended discharges in the atmosphere [11–22], are also accompanied by the simultaneous emission of intense UHF radiation in a broad frequency band, at least up to several gigahertz [23–28]. Note that the employment of the UHF emissions registered during extended discharges in the atmosphere potentially allows one to develop more accurate techniques for detailing the evolution of the discharge structures. The technical possibility of localizing the UHF radiation sources with centimeter accuracy was first demonstrated on the example of a laboratory discharge in [8].

However, to date, in-depth investigations of the generation regions of intense UHF radiation have not been carried out yet. The same applies to the statistical determination of the zones with the UHF radiation sources and their relationship with the discharge structures. Herein the key challenge is that the UHF radiation sources should be localized in the discharge with an accuracy close to the characteristic scale of single plasma structures and within time periods comparable to the characteristic evolution time of such structures, which can be of the order of hundreds of picoseconds. And this should be done simultaneously with the employment of fast discharge imaging to resolve the discharge structures in the region with the UHF radiation source. Thus, the basic concept proposing that colliding streamers emit intense UHF radiation remains questionable.

*parkevich@phystech.edu

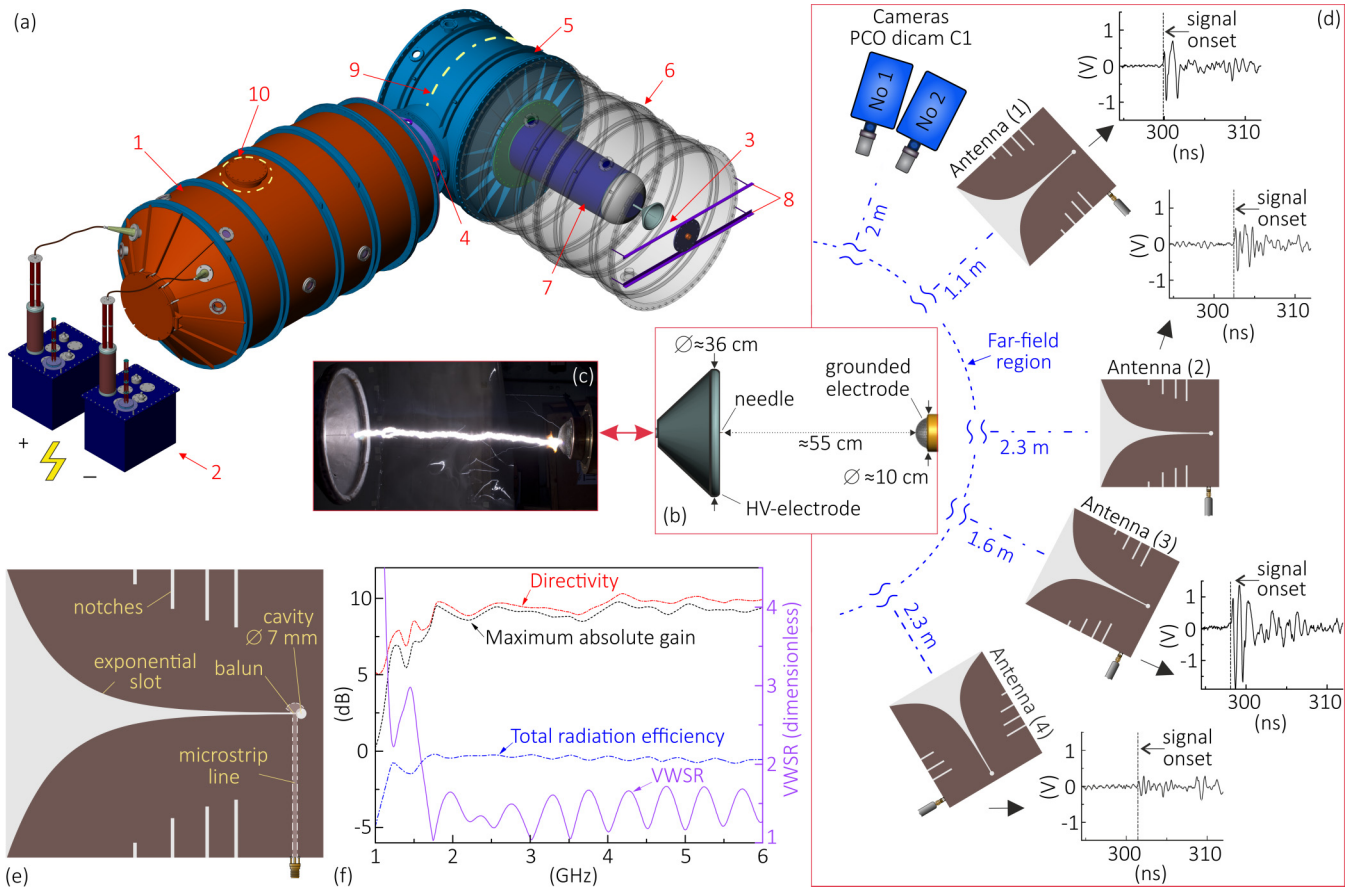


FIG. 1. Experimental setup: (a) pulse high-voltage installation, (b) investigated discharge gap, (c) integral photo of the resultant gap breakdown, (d) scheme of the device positions, (e) antenna design, and (f) antenna frequency characteristics.

In the study we tried to investigate this issue by carefully measuring the UHF emissions, localizing their regions in space, and imaging the discharge structures with a nanosecond resolution. The results were supplemented with the statistical observations of the streamer development, when varying the polarity of a high-voltage pulse (up to 1 MV) applied to an open air gap (approximately 55 cm in length) and initiated an electrical discharge. By employing a radio registration system, we determined the UHF emission regions with centimeter accuracy and resolved the discharge structures in these regions with a high temporal resolution using fast discharge imaging. The findings show that the generation mechanism of intense UHF radiation cannot be unambiguously associated with such basic processes as the head-on collision of opposite-polarity streamers or the interaction of single streamers with the near-electrode plasma at the surface of metal electrodes. It is found that the observed UHF emission appears basically as a precursor of the intense plasma development in a certain discharge region, whereinto a bright counterstreamer comes a bit later.

II. EXPERIMENTAL SETUP

A. High-voltage installation

The study was performed by using a pulse high-voltage (HV) installation [see Fig. 1(a)], which was the basis for the previous studies of various types of electromagnetic emissions

accompanying the development of an extended discharge in air [8,10,29–31]. The installation involves an oil-filled Marx generator (1) (with the maximum storage energy of about 60 mJ) connected to a high-voltage DC power supply (2) (negative or positive polarity) through a set of ballast resistors. When discharging, the Marx generator provides a HV pulse with the amplitude as high as 1 MV, which was supplied to the investigated discharge gap (3) through secondary coupling (4), oil-filled (5), and air (6) (shown transparent) sections of the installation along a central metal electrode hidden inside an oil-air bushing insulator (7). A HV electrode of the gap (3) was an extended metal cone (≈ 36 cm in diameter) with a needle (its output part is ≈ 1 cm in length) locked to the cone center [see Fig. 1(b)]. Opposite to the HV electrode at a distance of ≈ 55 cm a grounded hemispherical wire mesh electrode (≈ 10 cm in diameter) was placed, while being connected to a return-current circuit (8). The resultant breakdown of the gap occurs between its electrodes approximately along the discharge axis [see Fig. 1(c)]. The HV pulse applied to the discharge gap was registered by a capacitive-resistive voltage divider, its region is denoted as (9) in Fig. 1(a), inserted between the internal and external parts of the installation output. The divider was calibrated and has a temporal resolution of the order of several nanoseconds. When synchronizing the device signals, the delay of the voltage pulse traveling to the discharge gap was taken into account.

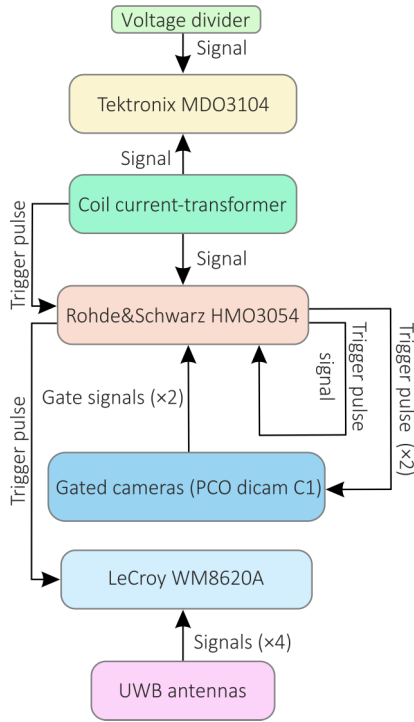


FIG. 2. Flowchart demonstrates the device triggering.

B. Device triggering and synchronization

The launching of the HV installation was controlled by using a coil current-transformer [its region is denoted as (10) in Fig. 1(a)], with its signal being split and employed to trigger the first two oscilloscopes: a Tektronix MDO3104 (1 GHz, 5 GSa/s) and a Rohde & Schwarz HMO3054 (500 MHz, 2 GSa/s); see the flowchart in Fig. 2. The Rohde & Schwarz oscilloscope in turn provides its own trigger pulse, which was also split to launch a LeCroy WM8620A oscilloscope (6 GHz, 20 GSa/s) together with two gated cameras. The Tektronix oscilloscope recorded the voltage divider and coil current-transformer signals. The Rohde & Schwarz oscilloscope recorded its split trigger pulse alongside the coil current-transformer and camera gate ($\times 2$) signals. The LeCroy oscilloscope recorded the ultrawideband (UWB) antenna signals ($\times 4$). In experiments we reduced to a single point in time the discharge voltage waveform, output signals of the camera gates, and the UWB antenna signals with the following timing errors: ≈ 2.5 ns for the discharge voltage signal, ≈ 0.5 ns for the ends of the camera gate signals, and ≈ 0.5 ns for the single onset of the UHF emission. The timing errors were driven by the oscilloscope discretizations, signal noisiness, uncertainty of the signal cable delays (measured with a 0.1-ns error), and the instability of the trigger pulse fronts. The mentioned errors are related to the device triggering only and do not take into account the localization accuracy of the UHF radiation source, which is considered in the separated section with the results discussed.

C. Discharge imaging

The discharge glow was registered by two scientific complementary metal oxide semiconductor (sCMOS) gated

intensified cameras (PCO dicam C1) both having a multiple-alkali-metal photocathode (S20), an output phosphor window (P46), and the shortest gate of 55 ns (the gate rises by approximately 10 ns when the delay of the camera triggering increases up to hundreds of nanoseconds). Each camera was coupled with a Canon EF 85-mm $f/1.8$ objective adjusted to the discharge gap from a distance of about 2 m at an angle of view of approximately 60° – 70° (with respect to the discharge gap axis) [see Fig. 1(d)]. Next to the objectives similar bandpass optical filters were placed to attenuate the plasma glow. The filters have transmission efficiency of up to 80% within 300–400 nm and of about 10% in the range 700–1000 nm. When imaging any stage of the discharge formation, the amplitude of the voltage pulses applied to the camera microchannel plates was maximal, and the camera sensitivity was controlled by changing the objective diaphragm only. The two cameras were synchronized with each other with an accuracy of ≈ 0.5 ns and in particular experiments recorded photos under similar conditions with a tunable delay ($\Delta\tau$, being of the order of several nanoseconds). The delay between the ends of two frames was determined as the time period between the instants the signals of the camera gates fall down up to the noise level. The time window (during $\Delta\tau$) of the discharge imaging was specified in calibration experiments by exposing the synchronized cameras to two 70-ps laser pulses (provided by a Lotis LS-2151 Nd:YAG laser) at 532 nm with different delays between the pulses. The latter were additionally controlled by using a fast photodetector DETO25A with a rise time of 150 ps. The timing accuracy of determining the resultant time window ($\Delta\tau$) between the two camera frames was ≈ 1 ns.

D. Registration of UHF radiation

The UHF emission during a high-voltage discharge was registered by four identical coplanar-type Vivaldi antennas with an exponential slot opening [32] [see Fig. 1(d)]. The slot is formed by the edges of an ≈ 18 - μm -thick copper layer deposited on an ≈ 1.52 -mm-thick substrate (RO4003CTM material) with a size of 22×20 cm². In the antenna a slotline is transited into a 50 Ω microstrip line coupled with a SMA (SubMiniature version A) connector. The geometry of the antenna elements (slot, cavity, balun) is shown in Fig. 1(e). Vertical notches of the dielectric substrate are used to dissipate surface currents induced along the lateral surface of the antenna by the incident radio wave. For the employed design of the antenna, according to the IEEE standard definitions of terms for antennas [33], the voltage standing wave ratio is within 1–2 at frequencies from 1.6 up to 6 GHz, with the total radiation efficiency (which includes conduction, dielectric, and impedance mismatch losses) being no higher than -0.23 dB [see Fig. 1(f)]. The antenna directivity varies from 5 to 10 dBi as the frequency increases from 1 to 6 GHz, whereas the first-null beam width of the major lobe rises from 80° to 180° . The maximum absolute gain at frequencies above 1.6 GHz is within 7–10 dB. The UWB antennas were connected to the LeCroy oscilloscope through SF-141 FEP low-loss cables (50 Ω , attenuation is no higher than 1.1 dB/m at frequencies below 6 GHz) with a length of ≈ 9 m, coupled with SMA attenuators (18 GHz, 40 dB attenuation). The

employed linearly polarized antennas were installed on dielectric tripods at different distances (>1 m) from the discharge gap center and registered UHF radiation with particular delays. The antennas were adjusted so that their major lobes were directed towards the discharge gap center, and the polarization of each antenna approximately coincides with the direction of the discharge gap axis. The antenna positions were measured with an accuracy of 0.5 cm. When synchronizing all device signals, for the UWB antenna signals we also took into account the estimated delay (≈ 1.23 ns) of the incident wave travel (70% of the speed of light in vacuum) in the antenna dielectric substrate along the slot up to the balun region, the measured delay (≈ 0.5 ns) of the wave travel along the antenna microstrip line, the geometric delay between the positions of the localized center of the UHF radiation source and the entrance of the antenna slot, and the space uncertainty in determining the source position. The geometric delays between the source center and entrance pupils of the camera objectives were taken into account in a similar way.

III. TECHNIQUES TO LOCALIZE UHF RADIATION SOURCES

A. Search for the signal points to solve the localization problem

Our study is aimed at identifying particular processes of the discharge development among all other processes emitting broadband radio emissions, which are related to the generation of intense UHF radiation. In this regard, we tried to resolve the discharge structures in the spatial regions, wherein the UHF emission arises for the first time [the very first burst; see Fig. 3(a)]. As the UHF emission starts, complex oscillations manifest themselves in the useful signals from the antennas after the very first burst. Nevertheless, in a number of events we were able to determine single bursts within useful signals [see Fig. 3(b)] and register the discharge structures in the spatial regions associated with such bursts. The analyzed bursts were associated with certain spatial regions understood as single sources of UHF radiation. The source positions were determined by solving the localization problem. To identify a single burst in the UHF radiation signals, we developed a special method based on the analysis of the spectral and temporal characteristics of the signals recorded in multiple shots. Following this method, for the very first burst, initially the first point above the noise level (its absolute amplitude is taken to be equal to the maximum amplitude of the signal fluctuations until the instant the UHF emission starts) is to be found in the curve of each useful signal [see the signal onsets in Fig. 3(a)]. Starting from the first point, basic patterns of the signal oscillations are looked for in a time period of about 1 ns. Such patterns should correlate with each other for the four antenna signals. A similar procedure was applied to identify bursts within useful signals [see Fig. 3(b)]. Since herein the first point is difficult to be selected, we additionally investigated time delays between the signals of UHF radiation emitted by the most probable generation regions of the radiation. Generally the basic patterns of the signal oscillations resemble the most common families of wavelets. A basic pattern is related to a single burst with a duration shorter than or of the order of 1 ns, which is supposed to be a characteristic of a single

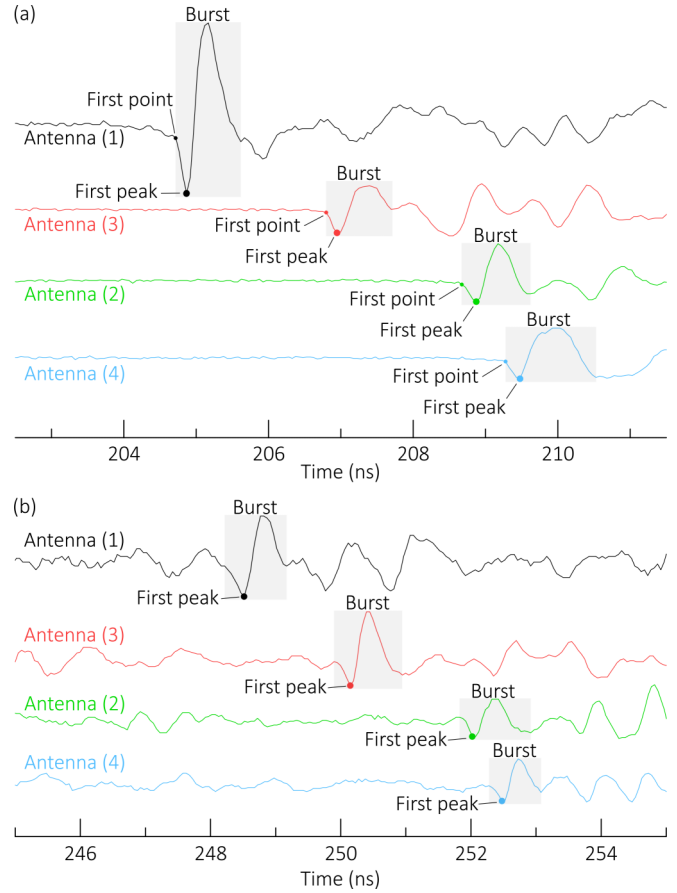


FIG. 3. Determination of the first peaks of the UHF radiation signals from four antennas for the (a) very first burst and (b) burst within useful signals. The first peaks are employed to obtain relative delays between the recorded signals and then solve the localization problem.

physical process of generating intense UHF radiation. The spectral and temporal structure of the basic pattern is changed over time, e.g., due to a stochastic manifestation of higher frequencies in the signals, but without the complete disappearance of the signal correlation. As the UHF emission decays (while being stipulated by a single process) or the interference of multiple sources occurs, the basic pattern is strongly distorted so that the signals from all antennas do not correlate. When analyzing the spectral and temporal characteristics of the signals, we noticed that independent sources can appear with a relative delay of about several hundred picoseconds even after the instant the UHF emission starts. By taking this fact into account, we found out that the best correlation is observed in the first beat of the burst, which can be assigned to the first peak [see Figs. 3(a) and 3(b)]. Statistics show that the signal amplitude in the time period between the very first point and first peak can increase by up to two orders of magnitude relative to the noise level, and the duration of such a period can range from one to several hundred picoseconds. In the particular case in Fig. 3(a) this period lasts for 150–200 ps; i.e., it is approximately equal for all signals. Note that the very process of generating UHF radiation develops probably much faster. For instance, the authors used a LeCroy oscilloscope

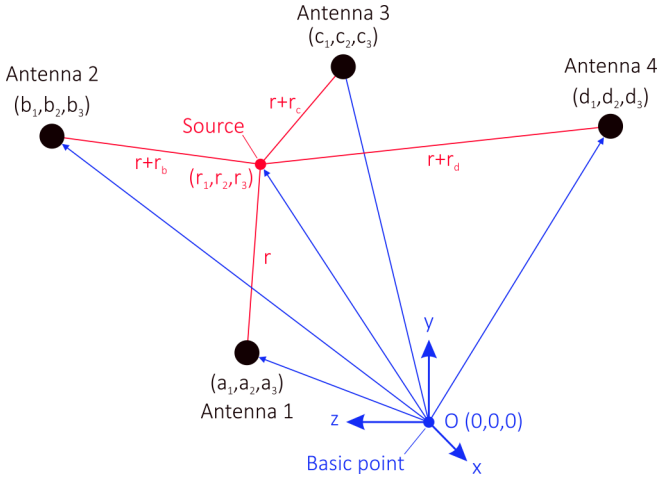


FIG. 4. Schematic representation of the source localization.

(16 GHz, 40 GSa/s) in [7] and showed that the front edges of certain bursts of UHF radiation can be as short as 25 ps. By taking into account the sharp rise in the signal amplitude and assuming the UHF emission to be the strongest starting from approximately the first peak, the moments corresponding to the first peaks were employed to determine relative delays Δt_{ij} (where $i, j = 1-4$) between the burst signals. Looking ahead, the discussed method to determine the relative delays provided very reliable results in the calibration experiments based on the localization of a compact handmade microwave generator with a known position in space. Notably, in the vicinity (± 50 ps) of the first peak the UHF radiation signals change very rapidly. One (sharp peak) or two points (smooth peak) are typically recorded in the vicinity of the first peak. If two points with similar signal amplitudes fall within the first peak region, the first point is accepted to be the first peak. Rarely, when three or four points (flat peak) fall within the first peak region, the second point is considered as the first peak. In experiments the uncertainty in determining the first peak was assumed to be ± 50 ps, which is reasonable in terms of the rapid changes in the signal amplitude in the vicinity of the first peak. Thus, the uncertainty in determining relative delay Δt_{ij} between two signals constituted 100 ps.

B. Statement of the localization problem

Let us state the localization problem. Note at once that the mathematical expressions given below are reduced to a form which is convenient for programming. The source (point with coordinates r_1, r_2 , and r_3) is assumed to appear as a region, with its dimensions being much smaller than all distances ($r, r + r_b, r + r_c$, and $r + r_d$) from the source to each antenna (see Fig. 4). The antenna coordinates are given as (a_1, a_2, a_3) , (b_1, b_2, b_3) , (c_1, c_2, c_3) , and (d_1, d_2, d_3) . The first antenna in Fig. 4 is closest to the UHF radiation source. Distance r from this antenna to the source is an unknown value which should be determined employing the coordinates of all antennas and relative time delays $r_b/c, r_c/c$, and r_d/c , where c is the speed of light in vacuum, between the measured radio signals.

Let us write down the corresponding equation system:

$$(a_1 - r_1)^2 + (a_2 - r_2)^2 + (a_3 - r_3)^2 = r^2, \quad (1)$$

$$(b_1 - r_1)^2 + (b_2 - r_2)^2 + (b_3 - r_3)^2 = (r + r_b)^2, \quad (2)$$

$$(c_1 - r_1)^2 + (c_2 - r_2)^2 + (c_3 - r_3)^2 = (r + r_c)^2, \quad (3)$$

$$(d_1 - r_1)^2 + (d_2 - r_2)^2 + (d_3 - r_3)^2 = (r + r_d)^2. \quad (4)$$

By subtracting each of expressions (2)–(4) from Eq. (1) and grouping the corresponding terms, equation system (1)–(4) can be reduced to a vector form

$$A\vec{s} = \vec{m} + \vec{p} \times r, \quad (5)$$

$$A = \begin{pmatrix} a_1 - b_1 & a_2 - b_2 & a_3 - b_3 \\ b_1 - c_1 & b_2 - c_2 & b_3 - c_3 \\ c_1 - d_1 & c_2 - d_2 & c_3 - d_3 \end{pmatrix}, \quad (6)$$

$$\vec{m} = \frac{1}{2} \times \begin{pmatrix} r_b^2 + \sum_{l=1}^3 (a_l^2 - b_l^2) \\ r_c^2 - r_d^2 + \sum_{l=1}^3 (c_l^2 - d_l^2) \\ r_b^2 - r_c^2 + \sum_{l=1}^3 (b_l^2 - c_l^2) \end{pmatrix}, \quad (7)$$

$$\vec{s} = \begin{pmatrix} r_1 \\ r_2 \\ r_3 \end{pmatrix}, \quad (8)$$

$$\vec{p} = \begin{pmatrix} r_b \\ r_c - r_b \\ r_d - r_c \end{pmatrix}, \quad (9)$$

for which the solution for the source coordinates is expressed in terms of the value of r ,

$$\vec{s} = A^{-1}\vec{m} + A^{-1}\vec{p} \times r, \quad (10)$$

where A^{-1} is the inverse matrix. By substituting source coordinates r_1, r_2 , and r_3 from (10) in (1), quadratic equation (11) and its solution (12) are derived:

$$\sum_{l=1}^3 (a_l - A_l^{-1}m_l - A_l^{-1}p_l \times r)^2 = r^2, \quad (11)$$

$$r = (-b + \sqrt{b^2 - 4ac})/2a, \quad \text{since } r > 0, \quad (12)$$

$$a = \sum_{l=1}^3 (A_l^{-1}p_l)^2 - 1, \quad (13)$$

$$b = 2 \times \sum_{l=1}^3 A_l^{-1}p_l \times (A_l^{-1}m_l - a_l), \quad (14)$$

$$c = \sum_{l=1}^3 (a_l - A_l^{-1}m_l)^2. \quad (15)$$

Here $a_l = (a_1, a_2, a_3)$, and $A_l^{-1}m_l$ and $A_l^{-1}p_l$ are the vector elements. Thus, by calculating expressions (11)–(15) with the employment of the measured coordinates of the four antennas and time delays, the source coordinates in expression (10) are found. The obtained solution of the localization problem is unambiguous and not overdetermined; i.e., all necessary and

sufficient input data are used (in this particular case, relative time delays $\Delta t_{12} = r_b/c$, $\Delta t_{13} = r_c/c$, and $\Delta t_{14} = r_d/c$).

C. Testing of the radio registration system

In the calibration experiments we tested the radio registration system by localizing the UHF emission produced by a compact microwave generator (with the voltage pulse amplitudes of the order of 10 kV and currents less than 1 mA) [see Figs. 5(a) and 5(b)]. In the case at hand, the calibration idea was somewhat similar to that widely used to calibrate (with the employment of a sounding balloon with a GPS receiver and radio transmitter) lightning mapping arrays and radio interferometers operating in the megahertz frequency range [34]. The high-voltage part (11) (filled with compound) of the handmade microwave generator in Fig. 5(a) was extracted from a portable electroshock weapon. The generator was powered by a battery (12) and discharged to a spark gap (14) with a length of about 1 cm by pressing a button (13). The spark gap was placed near the region with the geometric center (15) of the generator (its resultant dimensions are $7 \times 3.5 \times 4 \text{ cm}^3$). All generator contacts connected with wires (16) were insulated, and the generator itself was placed on a dielectric table (17) approximately in the center of the investigated discharge gap far from the metal electrodes. This was intentionally made to suppress the emission from the dipole image, which can be induced by the generator at any nearby metal surface and distort single bursts of UHF radiation employed to solve the localization problem. In the calibration experiments we assumed that both the spark (14) and internal elements of the high-voltage part (11) of the generator can radiate, i.e., the entire generator. Therefore, the spark gap (14) was placed near the geometric center (15) of the generator to reduce the uncertainty in determining the positions of the emission regions. The dielectric table (17) in turn was attached to the system of micrometer-precision translation stages located near the grounded base of the air section (6) of the HV installation in Fig. 1(a) at a distance of approximately 50 cm from the microwave generator. When the microwave generator is triggered, a spark originates in the gap (14), and the generation of UHF radiation starts. The emission lasts for about 400 ns at frequencies up to 6 GHz, with the highest radiation power being reached at frequencies within 1–2.5 GHz [see Figs. 5(c) and 5(d) and the inset]. The spectral data were obtained using the methods discussed in detail in the Appendix. The UHF radiation signals were recorded without attenuators because of their small amplitude. An important quality of the signals was that their rise time considered between the first point and first peak of the very first burst constituted about 100 ps, with the increase in the signal amplitude being two orders of magnitude relative to the noise level. Remarkably, we also tried to employ a laser spark in the focal plane of a lens as a small-sized source of microwave radiation, but no significant radiation at 1–6 GHz was obtained. Probably, the laser spark efficiently emits microwave radiation at very high frequencies, greater than 18 GHz [35].

In the calibration experiments five series of 50 events were considered. In each series the microwave generator had a similar position along the Y axis, with its extended part being directed along the Z axis. The geometric center of

the generator was shifted in the XZ plane (relative to the generator position in series 1) by different distances with a step of approximately 6 cm. Each point in the XZ and XY planes in Figs. 5(e) and 5(f) is associated with the very first burst identified within the UHF radiation signals by using the methods described in Secs. III A and III B. For each series the positions of the statistical centers of the localized sources were determined together with their standard deviations along the principle coordinate axes.

It is seen in Figs. 5(e) and 5(f) that even with the preliminary calibration of all signal paths (with a 100-ps error) and positions (with a 0.5-cm error) of the antennas the localization accuracy in determining the emission regions turns out to be quite good. All sources localized along the Y axis fall within the generator height (approximately 4 cm). Here the average standard deviation of the source positions relative to their statistical centers in all five series does not exceed approximately 0.6 cm. The largest spread (the average standard deviation is approximately 2 cm) of the sources is observed along the X axis. Notably, in all series the statistical centers of the localized sources do not coincide with the geometric center of the microwave generator. Each statistical center is distanced from the geometric center by approximately 3 cm, which points to a certain constant error in solving the localization problem. Such an error can be caused by the spread in the delays of the signal paths, which cannot be measured with an accuracy better than that allowed by the calibration experiments. Yet, the constant error can be minimized in the localization problem employing the calibration technique described in detail in the next section.

D. Corrections to relative time delays

The essence of the calibration task is as follows. Knowing the coordinates (x, y, z) of the geometric center of the UHF radiation source [which is assumed to coincide with the geometric center of the generator in Figs. 5(a), 5(b), 5(e), and 5(f)], antenna coordinates (x_i, y_i, z_i) , and relative time delays Δt_{ij} (where $i, j = 1-4$) between the signals recorded in 50 events, statistical corrections σ_{ij} to delays Δt_{ij} are to be found. Corrections σ_{ij} include all unknown spreads in the signal paths and antenna coordinates. Mathematically the calibration task consists in minimizing each of the six expressions

$$(R_i - R_j)/c - \Delta t_{ij} - \sigma_{ij} \longrightarrow 0, \quad (16)$$

$$R_i = \sqrt{(x - x_i)^2 + (y - y_i)^2 + (z - z_i)^2}, \quad (17)$$

$$R_j = \sqrt{(x - x_j)^2 + (y - y_j)^2 + (z - z_j)^2}, \quad (18)$$

where R_i and R_j are the distances from the source to the i and j antennas, for each event s of a particular measurement run. Corrections σ_{ij} are related to intrinsic delays $\sigma_1, \sigma_2, \sigma_3$, and σ_4 of the antennas as $\sigma_{12} = \sigma_1 - \sigma_2$, $\sigma_{13} = \sigma_1 - \sigma_3$, $\sigma_{14} = \sigma_1 - \sigma_4$, $\sigma_{23} = \sigma_3 - \sigma_2$, $\sigma_{24} = \sigma_4 - \sigma_2$, and $\sigma_{34} = \sigma_4 - \sigma_3$. The generalized form of the calibration task can be formulated as follows:

$$\overline{\text{RMS}} = \sqrt{\frac{1}{S} \sum_s \text{RMS}_s^2} \longrightarrow 0, \quad (19)$$

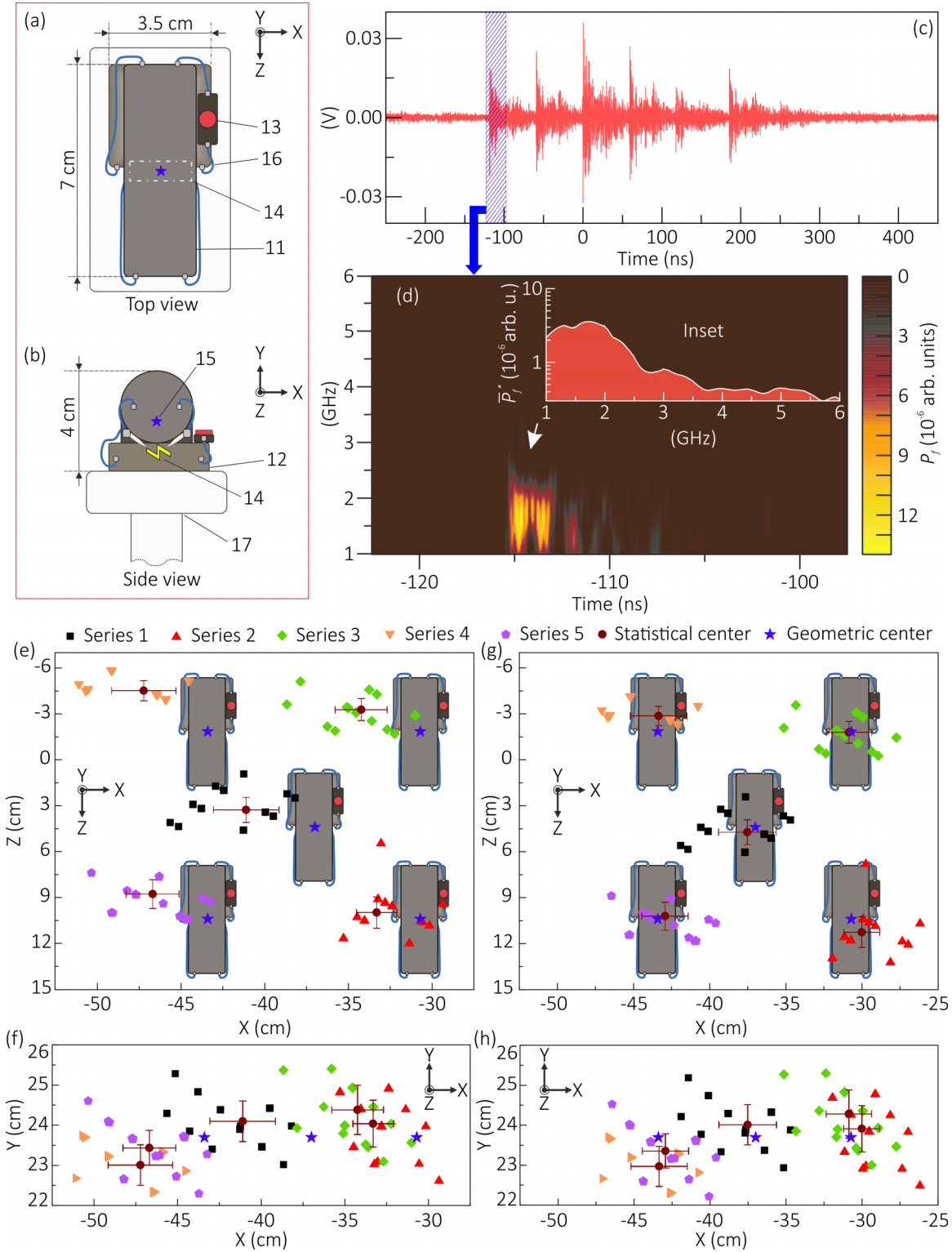


FIG. 5. Schematic representation of the microwave generator: (a) top view and (b) side view. (c) The typical UHF radiation signal and (d) its spectrogram obtained for a particular time period. The inset demonstrates a characteristic burst profile \bar{P}_f^* as a function of frequency f . The UHF radiation sources localized in five series of 50 events in the XZ and XY planes [(e), (f)] before and [(g), (h)] after the calibration of the radio registration system.

$$\text{RMS}_s = \sqrt{\frac{1}{6} \left[\sum_{i,j} (R_i - R_j)/c - \Delta t_{ij} - \sigma_{ij} \right]^2} \quad (20)$$

The parameter S equals the number of series multiplied by the six combinations of indices i and j in a single event s . Let us simplify expression (19) to the form more convenient for numerical calculations. Note that in Eq. (19) corrections σ_{ij}

are the variables; hence, $[(R_i - R_j)/c - \Delta t_{ij}]^2 = \text{const}$, and Eq. (19) can be replaced by the equivalent expression

$$\sum_s \sum_{i,j} [2\sigma_{ij}(R_i - R_j)/c - 2\Delta t_{ij}\sigma_{ij} + \sigma_{ij}^2] \longrightarrow 0. \quad (21)$$

Let us change the order of summation in (21):

$$\begin{aligned} & \sum_{i,j} \left(\left[2S\sigma_{ij}(R_i - R_j)/c - 2 \sum_s \Delta t_{ij} \right] \sigma_{ij} + S\sigma_{ij}^2 \right) \\ &= \sum_{i,j} (A_{ij}\sigma_{ij} + S\sigma_{ij}^2) \longrightarrow 0. \end{aligned} \quad (22)$$

Here matrix coefficient A_{ij} is introduced to simplify the expression. We now employ the fact that there are only three independent variables in Eq. (22), i.e., σ_{12} , σ_{13} , and σ_{14} ,

$$\begin{aligned} & \sum_{i,j} (A_{ij}\sigma_{ij} + S\sigma_{ij}^2) \\ &= A_{12}\sigma_{12} + S\sigma_{12}^2 + A_{13}\sigma_{13} + S\sigma_{13}^2 + A_{14}\sigma_{14} + S\sigma_{14}^2 \\ &+ A_{23}(\sigma_{13} - \sigma_{12}) + S(\sigma_{13} - \sigma_{12})^2 + \dots \longrightarrow 0, \end{aligned} \quad (23)$$

and we introduce new symbols

$$A_{12} - A_{23} - A_{24} = B_{12}, \quad (24)$$

$$A_{13} + A_{23} - A_{34} = B_{13}, \quad (25)$$

$$A_{14} + A_{24} + A_{34} = B_{14}. \quad (26)$$

Expression (23) then appears as

$$\begin{aligned} & \sum_{k=12:13:14} (B_k\sigma_k + 3S\sigma_k^2) \\ & - 2S(\sigma_{13}\sigma_{12} + \sigma_{14}\sigma_{12} + \sigma_{13}\sigma_{14}) \longrightarrow 0. \end{aligned} \quad (27)$$

Finally, expression (27) can be further simplified to the form

$$f(\vec{\sigma}) = \vec{\sigma} F \vec{\sigma}^T + \vec{\sigma} E \longrightarrow 0, \quad (28)$$

$$F = \begin{pmatrix} 3S & -S & -S \\ -S & 3S & -S \\ -S & -S & 3S \end{pmatrix}, \quad (29)$$

$$E = (B_{12} \ B_{13} \ B_{14})^T, \quad (30)$$

where $\vec{\sigma} = (\sigma_{12}, \sigma_{13}, \sigma_{14})$ is a vector, whose coordinates are required corrections σ_{12} , σ_{13} , and σ_{14} , and $\vec{\sigma}^T$ is a transposed vector $\vec{\sigma}$. Thus, we get the quadratic function $f(\vec{\sigma})$ of three variables.

The calibration task now consists in minimizing the function $\|f(\vec{\sigma})\| \longrightarrow 0$. It is an optimization problem, which we solve by using the gradient descent method. Notably, after all transitions made above, the function $\|f(\vec{\sigma})\|$ already has a quadratic form; therefore, the solution provided by the gradient descent method converges for any initial vector $\vec{\sigma}$ according to the Kantorovich relation. This fact greatly simplifies the optimization problem, since it eliminates the need to use more complicated and computationally intensive Levenberg-Marquardt or trust-region algorithms. To run the calculation of the optimization problem, the starting point $\vec{\sigma}_0$ is taken as zero, which is reasonable from an ideological point

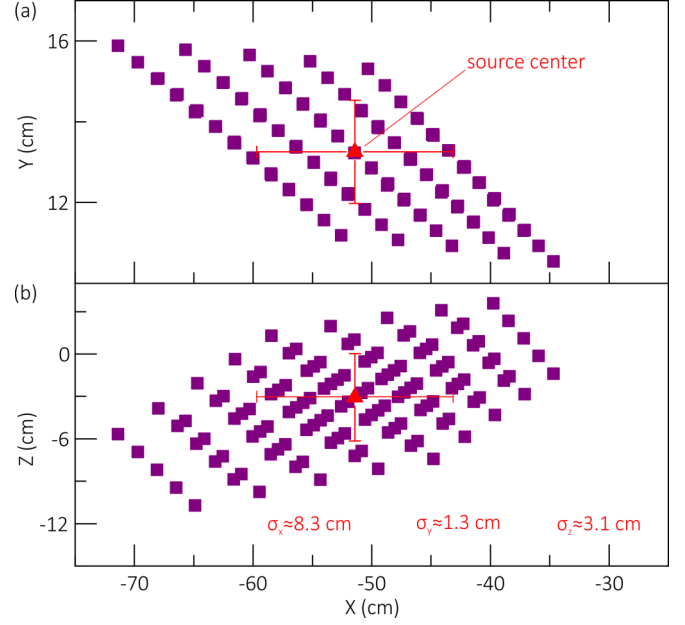


FIG. 6. Accuracy of determining the position of the UHF radiation source in the (a) XY and (b) XZ planes.

of view. As a result we obtain corrections σ_{12} , σ_{13} , and σ_{14} to relative delays Δt_{12} , Δt_{13} , and Δt_{14} used in Sec. III B.

Thus, we found out that for series 1–5 in Figs. 5(e) and 5(f) the best match between the positions of the statistical centers of the UHF radiation sources and the geometric center of the microwave generator is obtained with $\sigma_{12} \approx -40$, $\sigma_{13} \approx -55$, and $\sigma_{14} \approx 0$ ps [see the calibration results in Figs. 5(g) and 5(h)]. Notably, when calibrating the radio registration system, we performed additional tracing (with a 1-mm step) of all points in the generator volume to find the best match between the statistical centers of the localized sources in the five series and the selected points of the generator. For these points corrections σ_{ij} were also subsequently computed. The assumption that the most probable emission region coincides with the geometric center of the microwave generator turned out to be optimal for all series.

E. Resultant error of the source localization

In the previous section we determined corrections σ_{12} , σ_{13} , and σ_{14} to relative delays Δt_{12} , Δt_{13} , and Δt_{14} , which minimize the constant error of the source localization. By taking into account the corrections and the fact that the UHF radiation source sporadically originates in an extended discharge, the resultant error of the source localization is mainly governed by the accuracy of determining relative delays Δt_{12} , Δt_{13} , and Δt_{14} . Let us consider a specific example in Fig. 6. Herein a single source is localized for a certain event of the series in Fig. 5. The determined source position is marked as the source center in Fig. 6. The cloud of points around the source center is obtained by considering the 100-ps error in determining each relative delay Δt_{12} , Δt_{13} , and Δt_{14} (see the details in Sec. III A). We considered five cases of measuring the relative delay value: the deviations from the value obtained in experiments are ± 100 ps, ± 50 ps, and

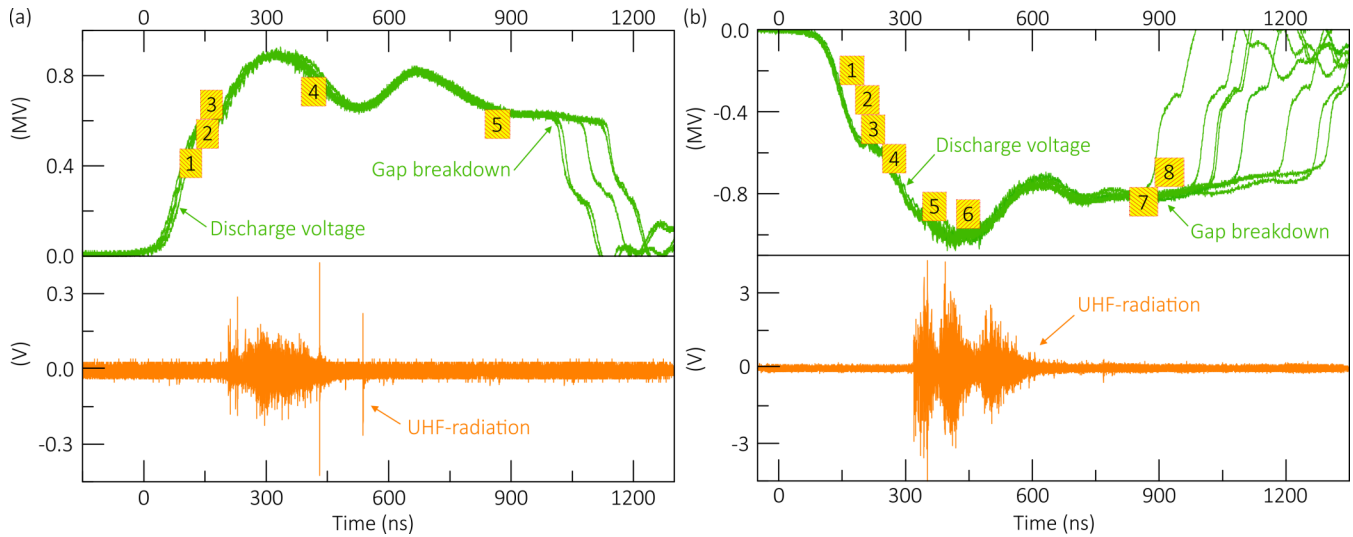


FIG. 7. Superimposed voltage waveforms and UHF radiation signals obtained in a number of shots for the (a) positive and (b) negative polarity of the HV pulse applied to the investigated discharge gap. Digits 1–8 in the voltage waveform indicate the time periods of the discharge imaging.

0, which correspond to 125 possible positions of the source in space. It is clearly seen in Fig. 6 that the nonoptimal angles [because of the design features of the employed HV installation—see Fig. 1(a)—and the limited space around it] of registering the UHF emission by the four antennas entail a significant spread in the possible positions of the source. In the particular case in Fig. 6 the radio registration system resolves the UHF radiation source with an error of approximately 8.3, 1.3, and 3.1 cm along the principal coordinate axes X , Y , and Z , respectively. Hereinafter, the localization error of a single source is described by the standard deviations of the possible positions of the source relative to its central position. This is reasonable since the vast majority of the possible source positions are concentrated near the source center. Each source is characterized by individual localization errors calculated for each of the principal coordinate axes. Thus, when determining the source position in the discharge, an ellipsoid bounding the source region is attributed to the source center.

IV. RESULTS

A. Characteristic development of the discharge

Figures 7(a) and 7(b) demonstrate the superimposed voltage waveforms and UWB antenna signals recorded in independent shots for the positive and negative polarity of the HV pulse applied to the investigated discharge gap in Fig. 1(b). For these shots the images of the discharge structures were obtained (see Figs. 8 and 9) in different time periods Δt_i ($i = 1, 2$) of the discharge evolution with an exposure time (exp) from 55 to 68 ns and objective diaphragms of $f/16$ – $f/8$. The images are presented in a color palette (256 shades of gray) and illustrate the characteristic development of the discharge in time and space. In each of Figs. 8 and 9 (top left corner) there is a basic frame of the discharge gap recorded with no discharge, which illustrates the angle of the gap imaging.

The first bright plasma structures of the discharge, while being a part of an extended streamer corona, emerge at the

HV electrode during the rise time (of about 200 ns) of the HV pulse tens of nanoseconds after its application (frame 1 in Figs. 8 and 9). Streamers develop from the HV electrode in a wide solid angle with characteristic velocities of the order of 10^8 cm/s, actively branch, and give rise to a complex net of plasma channels spanning almost the entire discharge gap (frame 2 in Figs. 8 and 9). During the propagation of primary streamers towards the grounded electrode the absolute amplitude of the discharge voltage increases to approximately 500–600 kV. The tails of certain growing streamers appear separated from a brightly shining corona locked to the HV electrode, which is clearly seen in the case of negative streamers in Fig. 9.

The character of the early stage of the discharge evolution is similar for both polarities of the applied HV pulse. When growing streamers come close to the grounded electrode, counterstreamers rapidly originate. For the positive polarity of the applied HV pulse counterstreamers often seemed to collide with primary streamers near the surface of the grounded electrode or at a short distance from it (frame 3 in Fig. 8). With the negative polarity, in contrast, counterstreamers start to propagate towards the HV electrode with characteristic velocities of $(1-4) \times 10^9$ cm/s, also actively branch (indeed, the closer counterstreamers come to the opposite electrode, the more intense they branch), and approach the HV electrode surface (frames 3–5 in Fig. 9). During the propagation of counterstreamers towards the opposite electrode the amplitude of the discharge voltage reaches the value of about 1 MV [Fig. 7(b)]. With the positive polarity of the applied HV pulse the maximum amplitude of the discharge voltage is slightly less, up to approximately 800 kV [Fig. 7(a)]. This can be stipulated by the different rates of the conductivity rise in the discharge plasma in the cases of the positive and negative polarity of the applied HV pulse, since the operating conditions of the Marx generator, denoted as (1) in Fig. 1(a), with positive and negative charging were similar. The plasma structure, which forms after the instant numerous streamers cross the entire discharge gap, has a high contrast but it

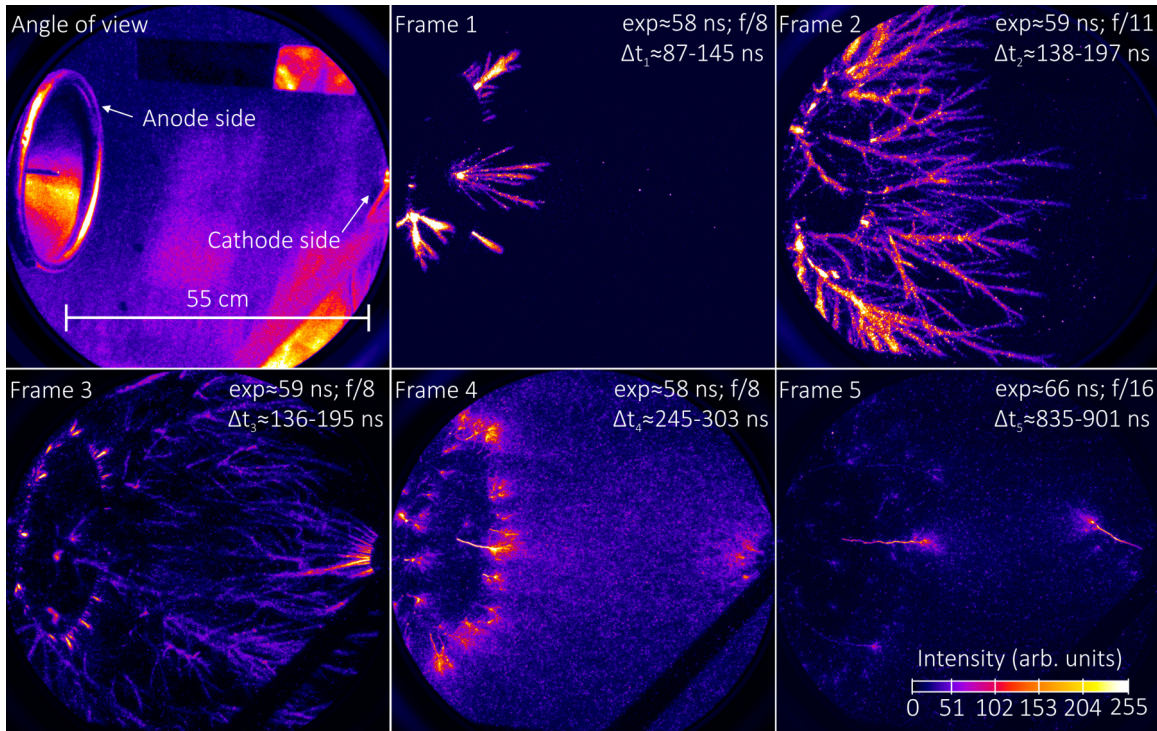


FIG. 8. Images (frames 1–5) demonstrating the discharge evolution for the positive polarity of the applied HV pulse in shots 1–5 in Fig. 7(a).

becomes more and more diffuse over time (frame 6 in Fig. 9). This is also observed within the streamer formation with the positive polarity of the applied HV pulse. The luminosity of a diffuse discharge becomes dim in the gap, and at a certain instant very bright narrow current channels, which are similar to high-current sparks [36–38], develop from the opposite electrodes (frames 4 and 7 in Figs. 8 and 9). At the heads of such channels bright diffuse coronas are resolved, which appear to be like the streamer coronas at the tops of leader channels (frames 5 and 7 in Figs. 8 and 9) [39–42]. The observed picture of narrow bright channels also seems to be similar to that of leaders developing in a lightning discharge [43–46]. The gap breakdown process (accompanied by a sharp drop in the gap voltage and an increase in the gap conductivity) is further associated with the growth of bright current channels and finally occurs when particular channels merge together somewhere in the discharge bulk (frame 8 in Fig. 9).

B. Spectral characteristics of the UHF emissions

The pre-breakdown stage of the discharge development lasts for about 1 μ s on average. At the same time the duration of the UHF emission takes about several hundred nanoseconds. The emission begins sharply in the discharge; the characteristic rise time of the very first burst is about 100 ps. From a statistical point of view the emission onset coincides with the stages when counterstreamers travel to the HV electrode (with the negative polarity of the applied HV pulse) or the first streamers come close to the grounded electrode (with the positive polarity of the applied HV pulse). The UHF emission is also observed during the formation of an

extended diffuse discharge in the gap, whereas the emission intensity gradually decays up to the appearance of narrow bright current channels. During the growing and merging of such channels the UHF emission is not observed in principle.

The UHF emission is represented by characteristic bunches with a duration of about 100 ns, which form the useful signals. Locally, the UHF emission is composed of multiple single bursts (in terms of the instantaneous power), with their duration being comparable to or shorter than 1 ns, which follow each other with a characteristic delay shorter than 1 ns on average (see also [8]). The amplitude of the UHF radiation signals detected with the positive polarity of the applied HV pulse is ten times less than that in the case of the discharge initiation by applying the HV pulse with the negative polarity. In both cases the highest power of the UHF radiation signals is often reached within the time period when the discharge voltage reaches its maximum value. Figures 10(a) and 10(b) illustrate typical UHF radiation signals registered with different polarities of the applied HV pulse and their temporal and spectral characteristics obtained by employing the methods discussed in detail in the Appendix. The spectrograms in Figs. 10(c) and 10(d) and insets 1 and 2 show that UHF radiation is characterized by frequencies in the entire range 1–6 GHz. From 1 to 6 GHz the characteristic power of the bursts decreases by a factor of approximately 3.5 and 8.8 for the positive and negative polarities of the applied HV pulse. Very high frequencies are concentrated directly in the time regions occupied by single bursts. In general terms the characteristics of UHF radiation generated by developing streamers in the extended discharge are similar to those of radio emissions produced by ordinary electric sparks [47].

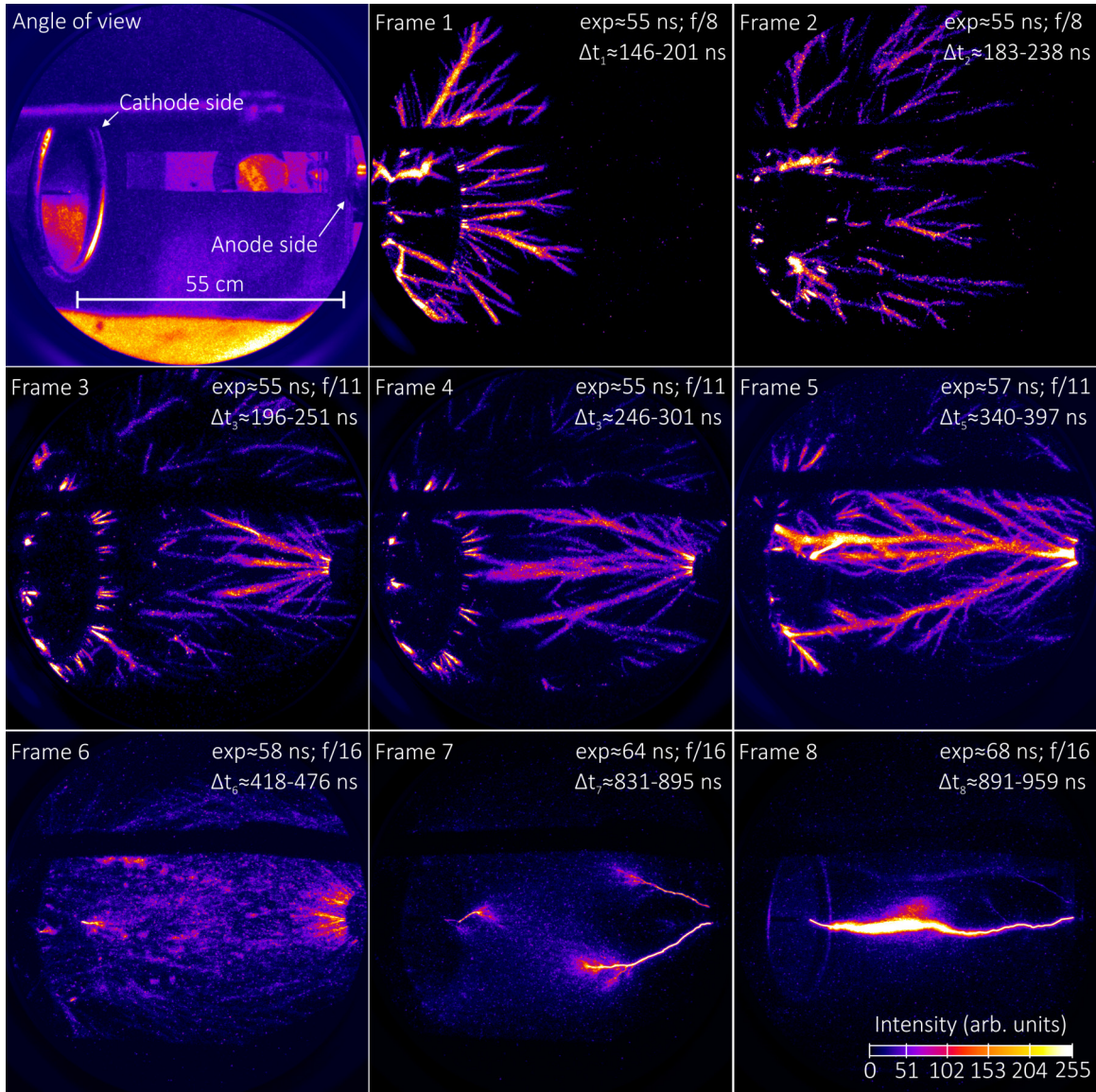


FIG. 9. Images (frames 1–8) demonstrating the discharge evolution for the negative polarity of the applied HV pulse in shots 1–8 in Fig. 7(b).

C. Statistical insight into the UHF emission regions

Figure 11 shows the distributions of the UHF radiation sources localized in the XY and XZ planes in the extended discharge for the positive and negative polarity of the HV pulse applied to the discharge gap in Fig. 1(b). The data were obtained in 52 (for the negative polarity) and 85 (for the positive polarity) independent events using the localization techniques described in Sec. III. The bar charts in Fig. 11 illustrate the statistics of the source observations along the discharge axis. The width of a single bin is 10 cm. The sources are presented as the space regions bounded by ellipsoids. The characteristic radii (averaged over the entire ensemble of the localized emission regions) of the ellipsoids along the principle coordinate axes X , Y , and Z are 5.8, 1.3, and 2.6 cm and 9.7, 1.3, and 3.3 cm for the positive and negative polarity of the applied HV pulse. It is seen that for both polarities the vast majority of the UHF radiation sources are concentrated

in the near-electrode regions. With the negative polarity many sources were localized inside the HV conical electrode. The spread of the source positions in the discharge periphery is essentially limited by the geometric dimensions of the conical electrode. With the positive polarity the largest number of sources are located in the near-electrode zone at a distance of about 10–20 cm from the grounded electrode surface. A number of sources were registered in the zones wherein the grounded electrode is fastened to the return-current circuit.

D. Emission regions resolved in single events

Figures 12–14 show the discharge structures resolved in the localized UHF emission regions for the positive (see Figs. 12 and 13) and negative (see Fig. 14) polarity of the applied HV pulse. The data are obtained in different shots. In the images the antenna signals are synchronized on the

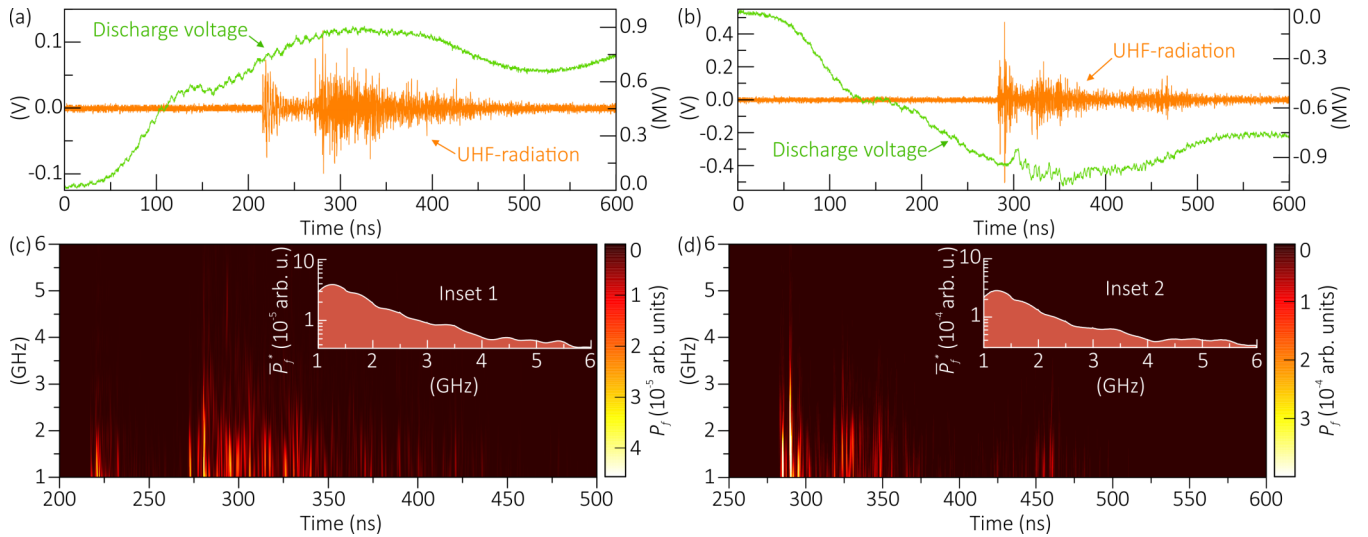


FIG. 10. Discharge voltage and typical UHF radiation signals registered for (a) positive and (b) negative polarity of the applied HV pulse. Spectrograms (c) and (d) show the spectrum evolution for the considered UHF radiation signals. Insets 1 and 2 illustrate a characteristic burst profile evaluated as a function of frequency in numerous events.

first captured burst of UHF radiation taking into account the signal timing for all diagnostic devices and geometric delays between the localized source and antennas (similarly for the two gated cameras). For each burst we additionally estimated its characteristic duration, which in the case at hand is understood as the time period when the signal amplitude is above the noise level, and the beats of the signals from all antennas correlate. The sizes of the ellipsoids in the frames, their positions, and orientations in space were calculated taking into account the exact angles of imaging by each camera and the perspective of the imaging system (estimated in the thin lens approximation).

In shot 51 in Fig. 12 three bursts of UHF radiation were localized. The first burst (approximately 1 ns in duration) is registered in the region wherein the grounded electrode is fastened to the return-current circuit [marked as 8 in Fig. 1(a)] in approximately 13 ns before the instant the first frame ends. The second burst (approximately 0.6 ns in duration) is detected near the center of the grounded electrode within the time window ($\Delta\tau \approx 5$ ns) of imaging by two cameras. The third burst (approximately 0.8 ns in duration) is also registered in the region wherein the grounded electrode is fastened to the return-current circuit approximately 9.5 ns after the end of the second frame. In shot 54 in Fig. 12 two bursts were localized. The first burst (approximately 0.7 ns in duration) is registered in approximately 8 ns before the end of the first frame, probably in the region wherein the streamer channel is subsequently connected with the grounded electrode. The second burst (approximately 0.9 ns in duration) is observed in the region wherein the grounded electrode is fastened to the return-current circuit approximately 3 ns after the end of the second frame. In shot 58 in Fig. 12 the first burst (approximately 0.95 ns in duration) is detected approximately 4 ns after the end of the second frame exactly in the region with a bright streamer channel connected with the grounded electrode. In this particular case the growing streamer reached the electrode surface within the time window ($\Delta\tau \approx 5$ ns) of imaging by two cameras. In shot 59 in Fig. 12 the first

burst (approximately 0.85 ns in duration) is registered near the surface of the grounded electrode in approximately 6 ns before the end of the first frame. Approximately 6–10 ns after the onset of the UHF emission a weak glow of the near-electrode plasma appears in the mentioned zone. In shot 55 in Fig. 13 the first burst (approximately 0.75 ns in duration) is registered in the region with the growing streamer at a distance of approximately 18 cm from the grounded electrode in approximately 7 ns before the end of the first frame. No brightly glowing counterstreamers propagating towards the UHF emission region from the side of the grounded electrode are observed in this case. There is only a weak plasma glow at the electrode surface. The second burst (approximately 0.9 ns in duration) in shot 55 in Fig. 13 is observed in the region wherein the grounded electrode is fastened to the return-current circuit approximately 15 ns after the end of the second frame.

In shot 9 in Fig. 14 the first burst (approximately 0.95 ns in duration) is detected near the edge of the cathode cone in approximately 22 ns before the end of the first frame. Here we observe the intense glow of the near-electrode plasma in the burst region shorted by the counterstreamer growing from the grounded electrode. In shot 13 in Fig. 14 the first burst (approximately 1 ns in duration) is registered approximately in the midgap approximately 8 ns after the end of the second frame. The UHF emission region falls within an extended bush of counterstreamers growing towards the HV electrode. No residual or secondary streamer channels from the HV electrode are clearly resolved in the localized UHF emission region in the first frame. In both shots 24 and 25 in Fig. 14 the first burst (approximately 1 ns in duration in both events) is registered approximately in the same zone at the edge of the cathode cone. The burst is observed in approximately 9 ns and 1.5 ns before the end of the first frame in shots 24 and 25, respectively. In the UHF emission region in shot 24 one can distinguish a brightly glowing channel of the counterstreamer, which reached the surface of the HV electrode. In the same zone in shot 25 before the end of the first frame the shorting

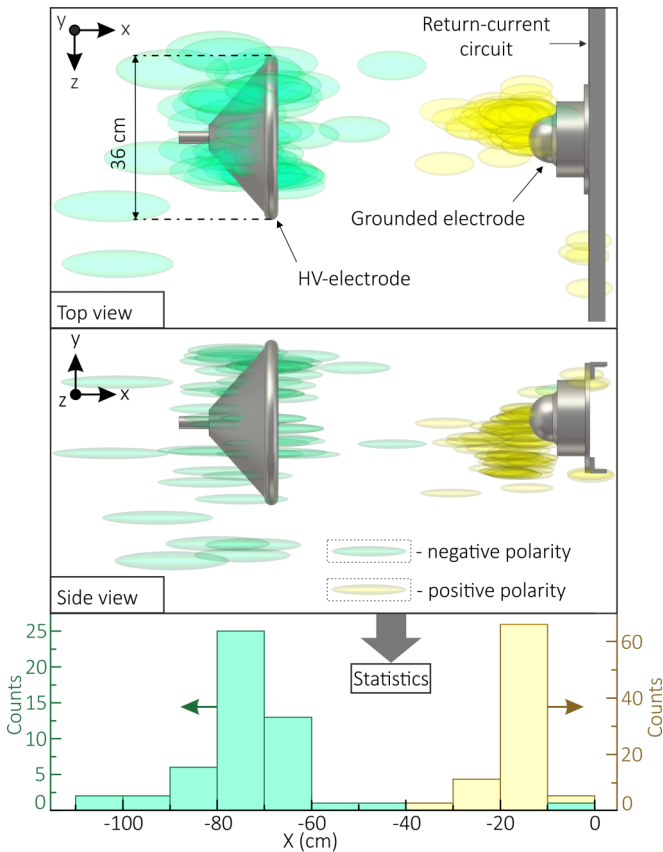


FIG. 11. The UHF emission regions localized in the discharge gap for the positive and negative polarity of the applied HV pulse. The source positions are presented in the XZ (top view) and XY (side view) planes. The bar charts show statistics of the source observations along the discharge axis. For the negative and positive polarity, counts are on the left and on the right.

of the near-electrode region by the counterstreamer is not yet observed, although the UHF emission has already occurred. The counterstreamer shorts the near-electrode region in the next several nanoseconds.

V. DISCUSSION

Let us consider the relationship between the localized UHF emission regions in Fig. 11 and the discharge development in Figs. 8, 9, 12–14. With the positive polarity of the applied HV pulse we register a weak glow of the near-cathode plasma when first streamers from the HV electrode (anode) approach the grounded electrode (cathode). This plasma gives rise to the subsequent development of counterstreamers from the cathode. In general first bright streamers short the near-cathode region during several nanoseconds (e.g., see shot 58 in Fig. 12). At the same time, even after the instant the near-cathode region is shorted, new counterstreamers continue to originate from the cathode. As a result multiple branching streamers arise in the zone with a length of about 20–30 cm near the cathode (see frame 3 in Fig. 8). The scale of such a zone is comparable to that of the region wherein the vast majority of the localized UHF radiation sources are concentrated (see Fig. 11). Based on the statistical data in Fig. 11,

the following assumption can be proposed. The generation mechanism of intense UHF radiation can be associated with the head-on collision (at a short distance from the cathode surface) of the cathode-directed streamer and counterstreamer originating from the cathode, or the interaction of the cathode-directed streamer with the near-cathode plasma at the metal electrode. Here we intentionally emphasize the complex structure of the near-electrode region since the assumption that the electrode can be considered as a single metal surface is a rough approximation. Experiments indicate that, when the first bright streamers come close to the cathode, the glowing near-cathode plasma originates. Remarkably, the authors of the study in [7] first provided experimental evidence that it is in the near-electrode regions of a laboratory discharge that intense UHF radiation is generated. In the study [8] we did not emphasize the role of the near-electrode regions in generating the UHF emissions, since we managed to localize a certain number of the UHF radiation sources far from the electrodes. However, as seen in Fig. 11, such emission regions are more an exception than the rule for a laboratory discharge.

A similar conclusion about the generation mechanism of intense UHF radiation suggests itself from the statistical data in Fig. 11 obtained for the negative polarity of the applied HV pulse, although in this case the character of the discharge development is somewhat different. The counterstreamers, which emerged at the grounded electrode (anode), cross the entire discharge gap and come close to the surface of the HV electrode (cathode) within several tens of nanoseconds (see frames 3–5 in Fig. 9). The growing counterstreamers actively branch and can in principle collide with any residual or secondary anode-directed streamer turned out in their travel way. This can happen in a wide region of the discharge gap. However, we observe that the primary streamers from the cathode expand into a wide solid angle and even beyond the discharge gap region by the instant the first counterstreamers emerge at the anode. Therefore, it is reasonable to assume that the counterstreamers from the anode can interact either with the near-cathode plasma at the metal electrode or with secondary streamers developing from the cathode. Such an assumption correlates with the distributions of the UHF emission regions and their spread in the region with the cathode cone in Fig. 11.

The idea of separating the possible triggers of the UHF emissions into such processes as the head-on collision of opposite-polarity streamers or the interaction of single streamers with the near-electrode plasma at the surface of metal electrodes appears to be statistically justified. However, we cannot unambiguously state that the detected UHF emissions are associated mainly with these basic processes. Moreover, the UHF emission regions analyzed in single shots (see Figs. 12–14) indicate that the generation mechanism of the emissions can be more complicated. Let us discuss a number of experimental facts. First, we often do not observe bright discharge structures exactly in the localized UHF emission region (e.g., see burst 1 in shots 51 and 54 in Fig. 12) and do not observe any discharge pattern indicating the head-on collision of opposite-polarity streamers far from the electrodes (e.g., see burst 1 in shot 55 in Fig. 13). In this regard the hypothesis that it is the head-on collision of opposite-polarity streamers (the glow of their plasma should manifest itself in the discharge images) produces intense UHF radiation is challenged.

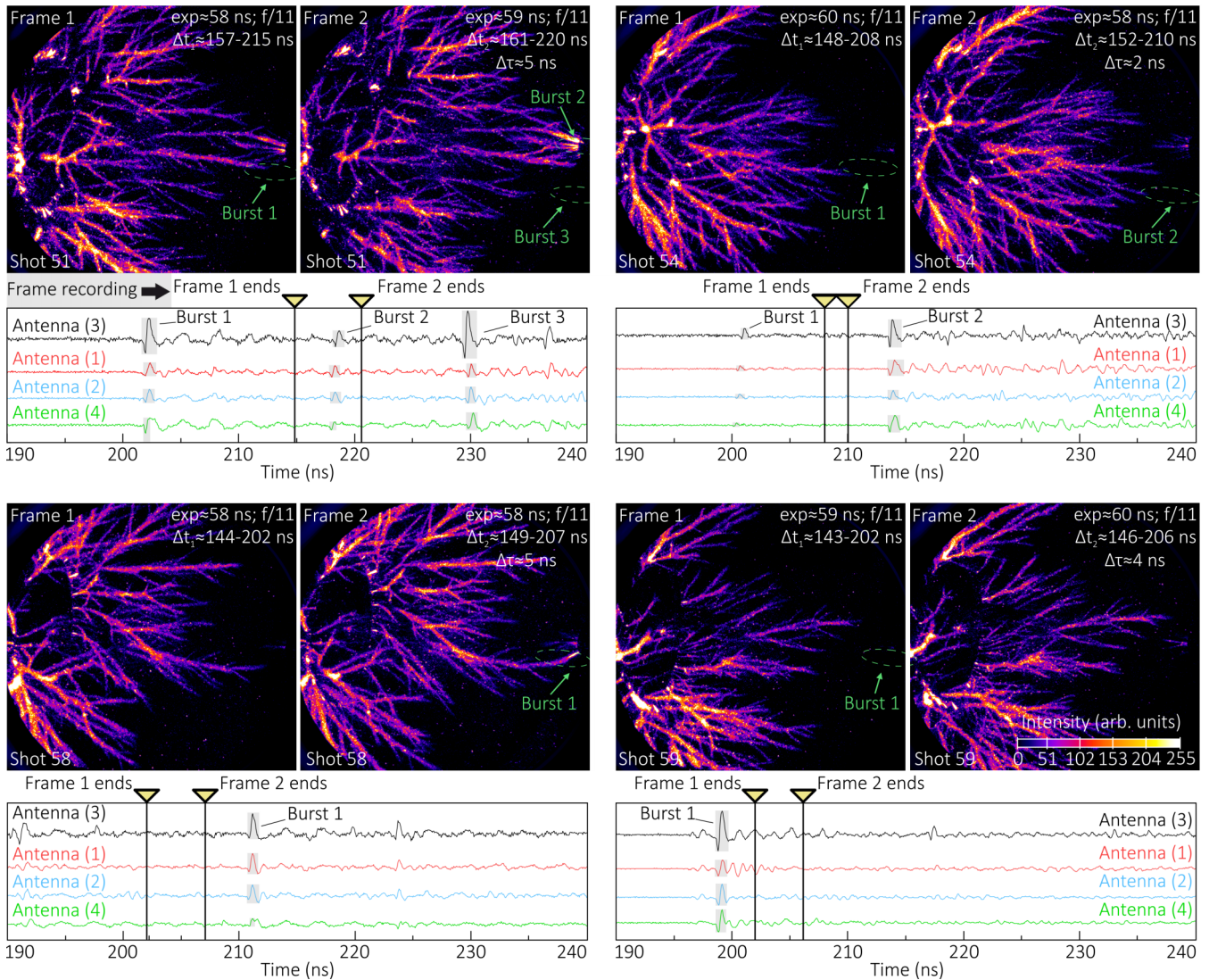


FIG. 12. Images demonstrate the discharge structures and localized UHF emission regions in single events for the positive polarity of the applied HV pulse.

Second, we observe that the shorting of the near-electrode region by bright plasma channels is not accompanied by the simultaneous emission of intense UHF radiation. For instance, in shot 58 in Fig. 12 the UHF emission occurred after the instant the near-cathode region was shorted by the bright plasma, although the emission region coincided in the first approximation with the zone with the bright plasma channel near the cathode. This is also the case for burst 2 in shot 51 in Fig. 12 and burst 1 in the shot in Fig. 14. Hence, the hypothesis that the streamer interaction with the near-electrode plasma at a metal electrode is accompanied by the emission of intense UHF radiation is also questionable.

Note that such processes as the collision of opposite-polarity streamers or the interaction of single streamers with plasma at the surface of metal electrodes can be considered in the approximation of a radiating dipole, with its electric moment being changed due to the change in the dipole length [7] or the movement of the dipole geometric center in space [48]. The dipole approximation used to describe the generation of intense UHF radiation, however, seems to be

inconsistent with the experimental results. The situation is similar with regards to other exotic mechanisms responsible for the UHF emissions, which are the generation of transition radiation within the passage of fast electron flows through boundary regions of the plasma-air medium [49], the emission of electromagnetic radiation by ionization waves propagating along plasma channels [50], and the analog of synchrotron radiation during the propagation of ionization waves along zigzag plasma channels [51]. According to these mechanisms, one can expect the UHF emission during the shorting of the near-electrode region by a single streamer. However, the emission can be observed either before or after this event. Also, it is doubtful that the generation mechanisms of intense UHF radiation in an extended discharge can be somewhat similar to those implemented in devices of microwave vacuum electronics (klystrons, magnetrons, traveling or backward wave tubes [52]), which involve modulated electron flows in an oscillatory system for pumping electromagnetic waves. One can assume the generation of intense UHF radiation to be associated with the development and enhancement of

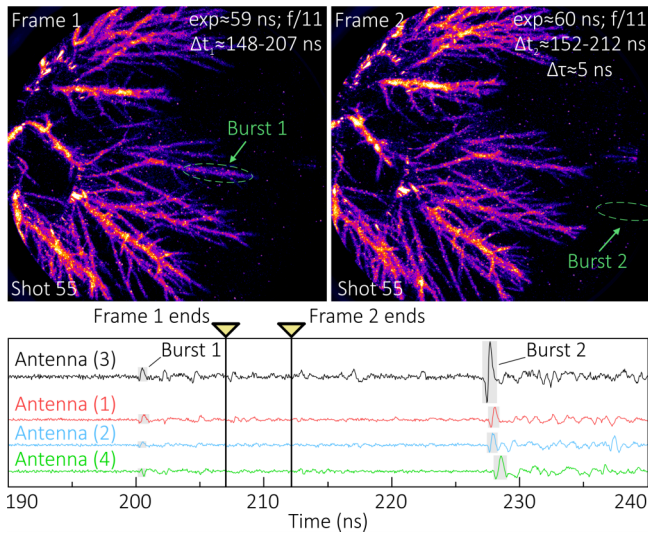


FIG. 13. Images demonstrate the discharge structures and localized UHF emission regions in single events for the positive polarity of the applied HV pulse.

collective plasma radiation processes [53–55], although it is unclear which plasma structures should be attributed to the localized regions of UHF radiation. There is the fact that brightly glowing plasma is often not observed in the UHF emission region. Therefore, the question arises as to what is the state of the discharge medium in the UHF emission region? This is an open question to be answered in future investigations.

In spite of the fact that the findings make the established concepts of generating intense UHF radiation in a high-voltage discharge untenable, our study allows one to look further into this phenomenon. We found that the observed region of the UHF emission serves as a precursor of the process of the intense plasma development in a certain discharge region, wherein a bright counterstreamer comes a bit later. This is the case for burst 1 in shots 51, 54, and 59 in Fig. 12 and burst 1 in shot 25 in Fig. 14. Our assumption seems especially convincing for shot 25. Herein the UHF emission was registered before the instant the emission region was shorted by the streamer from the anode. For burst 1 in shots 9 and 24 in Fig. 14 the assumption is valid if one considers the trajectory of the streamer development to be predetermined by certain physical processes played out in the UHF emission region. Certainly burst 1 in shot 55 in Fig. 12 and shot 13 in Fig. 14 seems to be unique. Such bursts are rare, but they do occur in the discharge. For them we do not exclude the possibility of the streamer collision with a certain plasma structure, although this structure is either invisible in the images (shot 55) or unresolved (shot 13) against the background of multiple growing streamers.

We would like also to mention a number of the observed features of the UHF emissions. With the negative polarity of the applied HV pulse it turned out to be very difficult to capture a single burst in the time window of imaging by the two gated cameras because of the sporadic development of the discharge and the random generation of the radio emissions. In addition numerous shots were discarded due

to the impossibility of localizing the very first burst or any burst within a useful signal. We found that with the negative polarity the signals from all antennas in most cases did not correlate. This was probably due to the fact that, when a single counterstreamer comes close to the corona (observed in the images for long time periods) burning at the cathode cone, independent UHF radiation sources appear almost simultaneously (within the first 100–200 ps after the useful signal onset) and radiate out of phase. This was rarely observed with the positive polarity owing to the more stable character of the streamer development. In experiments we also noticed that the first beat (employed to solve the localization problem; see Sec. III A) of the detected burst is similar to the first-order Gaussian wavelet, and the beat orientation directly depends on the polarity of the HV pulse applied to the discharge gap. With the positive polarity, all single bursts, which we localized, had a negative first peak, whereas with the negative polarity the first peak of the bursts was always positive. Perhaps this is obviously related to the change in the polarity of the current derivative in the generation region of UHF radiation. Remarkably, the mentioned difference in the first peak orientations also indicates that in experiments the UHF emission onset (in the vicinity of the first peak) driven by a certain physical process was identified correctly. In other words, we did not capture false oscillations of the UHF radiation signals in the region of the localized burst.

To sum up, we report the discovery of a certain physical process, which, among all other possible processes taking place in laboratory high-voltage discharges and capable of emitting broadband radio emissions, is accompanied by the generation of the strongest microwave radiation at frequencies above 1 GHz. This physical process is inconsistent with the established concepts of the generation of UHF radiation, in particular associated with those related to the interaction of opposite-polarity streamers with each other or near-electrode zones [1–5,7]. Certainly, more experiments with various experimental conditions (electrode geometry, voltage amplitudes, parameters of the discharge medium, etc.) need to be done to understand the nature of the localized regions with the UHF radiation sources. At the same time, our findings reveal a very complex physical picture of the UHF emission in a laboratory high-voltage discharge, which can turn out to be even more sophisticated for natural lightning phenomena. Notably, in ongoing atmospheric studies thunderstorms are comprehensively investigated through their remote sensing in the megahertz frequency range [21,56,57] complemented with the data of optical imaging [58,59] and acoustic synchronization [60,61]. The developed techniques [16,22,34,62–64] to analyze the radio emissions in this frequency range make it possible to localize the “fine structures” [18,19,65–68] of lightning discharges with an error of the order of several meters. At the same time, the transition to the technique of registering the UHF emissions can significantly advance the ability to localize lightning discharge processes with an accuracy close to units of centimeters. However, there were still no attempts to localize the UHF radiation sources at frequencies above 1 GHz in thunderstorms because of many technical challenges. In this regard now it is impossible to draw any unambiguous conclusions on the relationship between the UHF radiation sources observed in a laboratory experiment

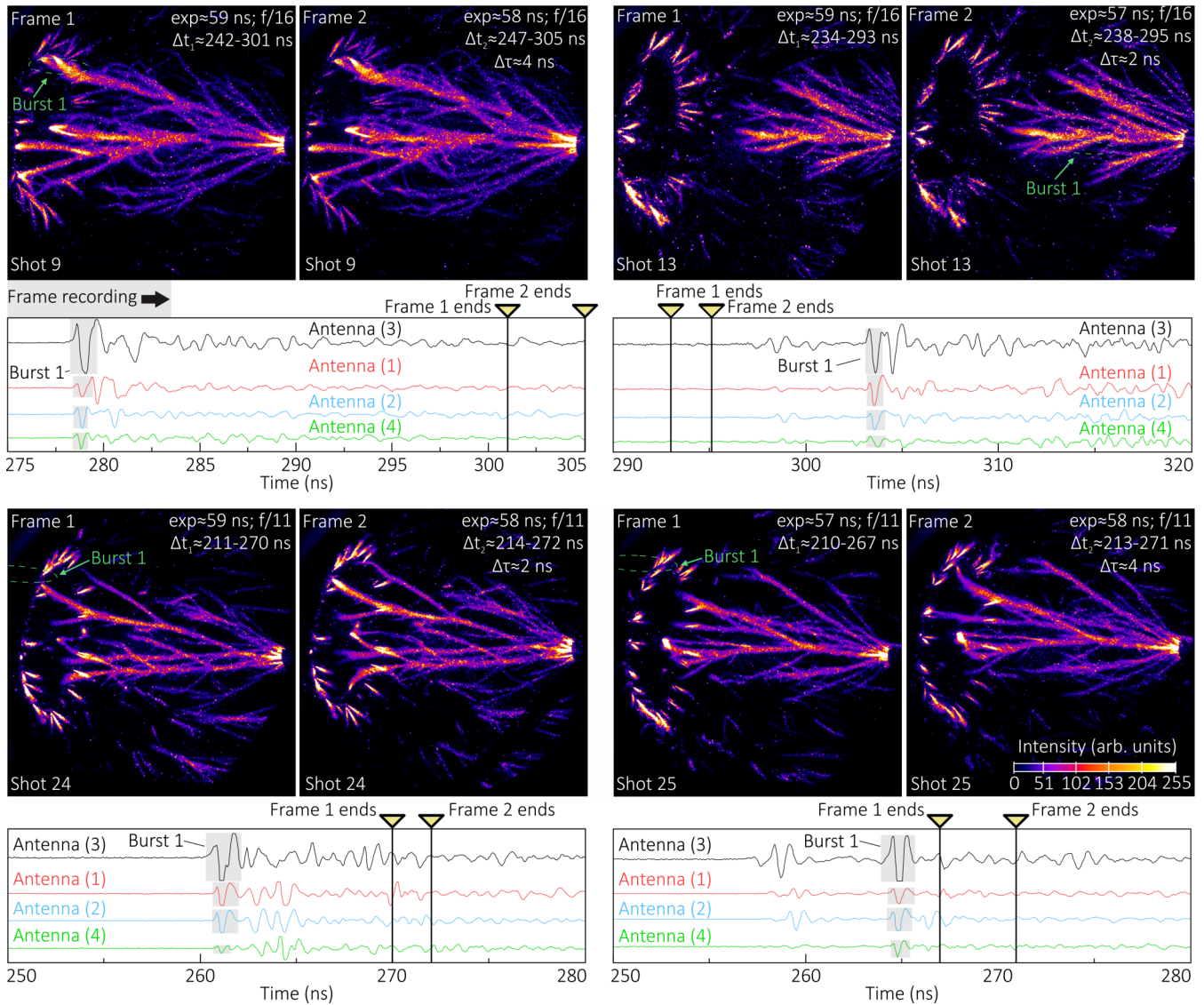


FIG. 14. Images demonstrate the discharge structures and localized UHF emission regions in single events for the positive polarity of the applied HV pulse.

and those occurring in atmospheric discharges. Therefore, any research in this field is in great demand. We hope that the techniques for precise localization of the UHF radiation sources developed in this study can serve as efficient tools in subsequent researches aimed at revealing features of both the thunderstorm development and accompanying broadband radio emissions.

VI. CONCLUSION

Let us briefly summarize the results obtained. In the study we developed the algorithm for searching the points of the UHF radiation signals employed to solve the localization problem. The algorithm is based on the in-depth analysis of the spectral and temporal characteristics of the UHF radiation signals in multiple events. We developed the radio registration system based on the four UWB antennas and tested it using the compact microwave generator created specifically for this task. The special calibration technique was imple-

mented to minimize the constant error in the localization problem, which allowed one to determine the corrections to the relative time delays between the UHF radiation signals with picosecond accuracy. The radio registration system was calibrated employing the data on the localized regions of the UHF emissions, which were produced by the created microwave generator. It is shown that the UHF radiation sources are localized with centimeter accuracy in extended discharges. The characteristic dynamics of the discharge development and its temporal correlation with the UHF emissions are described. The intense UHF radiation is found to be generated during several hundred nanoseconds at the pre-breakdown stage of the discharge formation, which lasts for about 1 μ s. Statistics show that the UHF emission onset coincides with the discharge stages when counterstreamers, originated from the grounded electrode, travel to the HV electrode (with the negative polarity of the applied HV pulse) or the first streamers from the HV electrode approach the grounded electrode (with the positive polarity of the applied HV pulse). It is mentioned

that the UHF emission is also observed during the formation of an extended diffuse discharge in the gap, whereas the emission intensity gradually decays up to the appearance of narrow bright current channels similar to long sparks. During the growing and merging of such channels the UHF emission is not observed. By employing the developed methods to obtain the data on the spectral and temporal characteristics of the UHF radiation signals, it is demonstrated that the registered UHF emissions are composed of multiple single bursts, with their duration being comparable to or shorter than 1 ns, which follow each other with a characteristic delay shorter than 1 ns on average. The observed UHF emissions are characterized by frequencies within 1–6 GHz, with the characteristic power of the bursts being decreased from 1 to 6 GHz by a factor of approximately 3.5 and 8.8 for the positive and negative polarities of the applied HV pulse. Very high frequencies are concentrated directly in the time regions occupied by single bursts as well. The distributions of the localized UHF radiation sources are obtained for both polarities of the HV pulse applied to the long discharge gap. It is shown that from a statistical point of view with both polarities the vast majority of the sources are concentrated in the near-electrode regions. In the example of single shots the characteristic dynamics of the discharge structure in the localized UHF emission regions is demonstrated. It is found that the generation mechanism of intense UHF radiation in a laboratory high-voltage discharge cannot be unambiguously associated with such basic processes as the head-on collision of opposite-polarity streamers or the interaction of single streamers with the near-electrode plasma at the surface of metal electrodes. We discovered that the observed region of the UHF emission serves as a precursor of the process of the intensive plasma development in a certain discharge region, whereinto a bright counterstreamer comes a bit later.

Thus, the study reveals the interesting phenomena accompanying the development of a laboratory atmospheric discharge. The findings provide a deeper insight into the radio emissions driven by the streamer formation processes. The data obtained on the UHF emissions can be helpful in investigating broadband radio emissions generated in thunderstorms.

ACKNOWLEDGMENT

The study was supported by the Russian Science Foundation (Grant No. 23-19-00524).

APPENDIX: SIGNAL PROCESSING

The registered UHF radiation signals are broadband, and single bursts of such an electromagnetic emission follow each other rapidly over hundreds of nanoseconds. At the same time, to provide a deeper insight into the UHF emissions, their frequency characteristics should be localized in time, while preserving a reliable resolution in both the time and frequency domains according to the uncertainty principle, $\Delta f \times \Delta T \geq 1$. A single burst is considered as a process with duration ΔT

and effective bandwidth Δf , which contains about 90% of the signal energy concentrated in ΔT . It was established in [8] that the majority of bursts have a duration shorter than 1 ns, with a delay between adjacent bursts being also no longer than 1 ns. Therefore, it is reasonable to evaluate the burst frequency characteristics in time periods no longer than 1 ns, i.e., to resolve the basic structure of the signals, understanding that the spectral resolution is bounded from below at 1 GHz. Nevertheless, it is advantageous in terms of the frequency response of the employed UWB antennas [see Fig. 1(f)].

By taking into account the noted facts, we developed a practical method (closely related to the idea of the short-time Fourier transform) to localize the frequency characteristics of the UHF emissions in time, the main essence of which is as follows. The time interval Δ of a useful signal is first determined. A short time period $\Delta^* = [t_k - T^*; t_k + T^*]$, the duration of which is 1 ns ($T^* = 0.5$ ns), is then defined for each time point t_k in Δ . By switching to instantaneous power $P(t)$ of the signal, we perform a Fourier transform \mathcal{F} in each introduced time interval Δ^* . To improve the estimation of the signal spectrum and reduce edge effects, each time interval Δ^* is expanded up to Δ and supplemented with time points having zero power values. After this procedure an inverse Fourier transform $P_{f^*} = \mathcal{F}^{-1}(\mathcal{F}(P(t)))|_{f^*}$ is applied for particular harmonic f^* , and a continuous function P_f is constructed employing obtained values P_{f^*} , which are attributed to a particular time point t_k . The smoothness of $P_f(t)$ is achieved by evaluating it with a frequency step of 10 MHz. The discussed procedure is performed for each time point t_k with a 50-ps time step. The obtained distributions of $P_f(t)$ are then employed to construct a continuous map (spectrogram) of the signal spectrum, which describes the local trend in the instantaneous power of the UHF radiation signal in the time and frequency domains (see Figs. 5 and 10). The spectrogram intensity is given in a color palette and clearly demonstrates the evolution of the dominant frequency components of the UHF radiation signal. Notably, the signal attenuation in the employed cables was evaluated and taken into account when computing the spectrograms.

By constructing spectrograms, we also calculate the characteristic burst profile \bar{P}_f^* as a function of frequency f . To this end, spectrograms for numerous UHF radiation signals are obtained and subjected to tracing in the narrow frequency interval $\Delta f^* = 10$ MHz. In each interval Δf^* we look for power maxima $\bar{P}_{\Delta f^*}^{\max}$ above the noise level (computed for each Δf^*), which fulfill the following criterion: there is no secondary maximum in t_{FWHM} (full width at half maximum) introduced for the considered maximum. The criterion is used to exclude bursts which are merged together, e.g., because of the interference of numerous sources. The resultant burst profile is computed as average $\bar{P}_f = 1/M \sum_{m=1}^M \bar{P}_m^{\max}(\Delta f^*)$, where M is the total number of all bursts resolved in Δf^* . The corresponding burst profiles can be found in Figs. 5 and 10.

- [1] J. R. Dwyer and M. A. Uman, The physics of lightning, *Phys. Rep.* **534**, 147 (2014).
 [2] M. A. Ihaddadene and S. Celestin, Increase of the electric field in head-on collisions between negative

and positive streamers, *Geophys. Res. Lett.* **42**, 5644 (2015).

- [3] L. Babich and E. Bochkov, Numerical simulation of electric field enhancement at the contact of positive and negative

- streamers in relation to the problem of runaway electron generation in lightning and in long laboratory sparks, *J. Phys. D* **50**, 455202 (2017).
- [4] F. Shi, N. Liu, J. R. Dwyer, and K. M. Ihaddadene, VHF and UHF electromagnetic radiation produced by streamers in lightning, *Geophys. Res. Lett.* **46**, 443 (2019).
- [5] J. Koile, N. Liu, and J. Dwyer, Radio frequency emissions from streamer collisions in subbreakdown fields, *Geophys. Res. Lett.* **48**, e2021GL096214 (2021).
- [6] M. Gushchin, S. Korobkov, I. Y. Zudin, A. Nikolenko, P. Mikryukov, V. Syssoev, D. Sukharevsky, A. Orlov, M. Y. Naumova, Y. A. Kuznetsov *et al.*, Nanosecond electromagnetic pulses generated by electric discharges: Observation with clouds of charged water droplets and implications for lightning, *Geophys. Res. Lett.* **48**, e2020GL092108 (2021).
- [7] I. Zudin, M. Gushchin, I. Verzhinin, S. Korobkov, P. Mikryukov, A. Strikovskiy, A. Nikolenko, A. Belov, V. Syssoev, A. Orlov *et al.*, Amplitude-temporal and spectral characteristics of pulsed UHF-SHF radiation of a high-voltage streamer discharge in air under the atmospheric pressure, *Energies* **15**, 9425 (2022).
- [8] E. V. Parkevich, A. I. Khirianova, T. F. Khiryanov, I. S. Baidin, K. V. Shpakov, A. A. Rodionov, Ya. K. Bolotov, V. A. Ryabov, Y. K. Kurilenkov, I. S. Samoylov, S. A. Ambrozevich, and A. V. Oginov, Electromagnetic emissions in the MHz and GHz frequency ranges driven by the streamer formation processes, *Phys. Rev. E* **106**, 045210 (2022).
- [9] J. Montanyà, F. Fabró, V. March, O. van der Velde, G. Solà, D. Romero, and O. Argemí, X-rays and microwave RF power from high voltage laboratory sparks, *J. Atmos. Sol. Terr. Phys.* **136**, 94 (2015).
- [10] E. V. Parkevich, K. V. Shpakov, I. S. Baidin, A. A. Rodionov, A. I. Khirianova, T. F. Khiryanov, Y. K. Bolotov, M. A. Medvedev, V. A. Ryabov, Ya. K. Kurilenkov, and A. V. Oginov, Streamer formation processes trigger intense x-ray and high-frequency radio emissions in a high-voltage discharge, *Phys. Rev. E* **105**, L053201 (2022).
- [11] X.-M. Shao, D. Holden, and C. Rhodes, Broad band radio interferometry for lightning observations, *Geophys. Res. Lett.* **23**, 1917 (1996).
- [12] T.-O. Ushio, Z.-I. Kawasaki, Y. Ohta, and K. Matsuura, Broad band interferometric measurement of rocket triggered lightning in Japan, *Geophys. Res. Lett.* **24**, 2769 (1997).
- [13] Z. Kawasaki, R. Mardiana, and T. Ushio, Broadband and narrowband RF interferometers for lightning observations, *Geophys. Res. Lett.* **27**, 3189 (2000).
- [14] P. R. Krehbiel, R. J. Thomas, W. Rison, T. Hamlin, J. Harlin, and M. Davis, Lightning mapping observations in central Oklahoma, *Eos* **81**, 21 (2000).
- [15] S. J. Goodman, R. Blakeslee, H. Christian, W. Koshak, J. Bailey, J. Hall, E. McCaul, D. Buechler, C. Darden, J. Burks *et al.*, The North Alabama Lightning Mapping Array: Recent severe storm observations and future prospects, *Atmos. Res.* **76**, 423 (2005).
- [16] M. Stock, M. Akita, P. Krehbiel, W. Rison, H. Edens, Z. Kawasaki, and M. Stanley, Continuous broadband digital interferometry of lightning using a generalized cross-correlation algorithm, *J. Geophys. Res.: Atmos.* **119**, 3134 (2014).
- [17] J. N. Tilles, N. Liu, M. A. Stanley, P. R. Krehbiel, W. Rison, M. G. Stock, J. R. Dwyer, R. Brown, and J. Wilson, Fast negative breakdown in thunderstorms, *Nat. Commun.* **10**, 1648 (2019).
- [18] B. Hare, O. Scholten, J. Dwyer, T. Trinh, S. Buitink, S. Ter Veen, A. Bonardi, A. Corstanje, H. Falcke, J. Hörandel *et al.*, Needle-like structures discovered on positively charged lightning branches, *Nature (London)* **568**, 360 (2019).
- [19] B. M. Hare, O. Scholten, J. Dwyer, U. Ebert, S. Nijdam, A. Bonardi, S. Buitink, A. Corstanje, H. Falcke, T. Huege *et al.*, Radio Emission Reveals Inner Meter-Scale Structure of Negative Lightning Leader Steps, *Phys. Rev. Lett.* **124**, 105101 (2020).
- [20] W. Yin, W. Jin, C. Zhou, Y. Liu, Q. Tang, M. Liu, G. Chen, and Z. Zhao, Lightning detection and imaging based on VHF radar interferometry, *Remote Sensing* **13**, 2065 (2021).
- [21] O. Scholten, B. M. Hare, J. Dwyer, N. Liu, C. Sterpka, I. Kolmašová, O. Santolik, R. Lan, L. Uhlř, S. Buitink *et al.*, Interferometric imaging of intensely radiating negative leaders, *Phys. Rev. D* **105**, 062007 (2022).
- [22] X.-M. Shao, D. Jensen, C. Ho, P. Graham, W. Haynes, M. Caffrey, E. Raby, C. Meierbachtol, D. Hemsing, and R. Sonnenfeld, Three-dimensional broadband interferometric mapping and polarization (BIMAP-3D) observations of lightning discharge processes, *J. Geophys. Res.: Atmos.* **128**, e2022JD037955 (2023).
- [23] F. Horner and P. Bradley, The spectra of atmospheric discharges, *J. Atmos. Terr. Phys.* **26**, 1155 (1964).
- [24] M. Brook and N. Kitagawa, Radiation from lightning discharges in the frequency range 400 to 1000 Mc/s, *J. Geophys. Res.* **69**, 2431 (1964).
- [25] K. Zonge and W. Evans, Prestroke radiation from thunderclouds, *J. Geophys. Res.* **71**, 1519 (1966).
- [26] E. Kosarev, V. Zatsepin, and A. Mitrofanov, Ultrahigh frequency radiation from lightnings, *J. Geophys. Res.* **75**, 7524 (1970).
- [27] R. Harvey and E. Lewis, Radio mapping of 250- and 925-megahertz noise sources in clouds, *J. Geophys. Res.* **78**, 1944 (1973).
- [28] V. Fedorov, Y. A. Frolov, and P. Shishkov, Millimetric electromagnetic radiation of a lightning return stroke, *J. Appl. Mech. Tech. Phys.* **42**, 392 (2001).
- [29] A. V. Agafonov, A. V. Bagulya, O. D. Dalkarov, M. A. Negodaev, A. V. Oginov, A. S. Rusetskiy, V. A. Ryabov, and K. V. Shpakov, Observation of Neutron Bursts Produced by Laboratory High-Voltage Atmospheric Discharge, *Phys. Rev. Lett.* **111**, 115003 (2013).
- [30] A. Agafonov, V. Bogachenkov, A. Chubenko, A. Oginov, A. Rodionov, A. Rusetskiy, V. Ryabov, A. Shepetov, and K. Shpakov, Observation of hard radiations in a laboratory atmospheric high-voltage discharge, *J. Phys. D* **50**, 165202 (2017).
- [31] A. Agafonov, A. Oginov, A. Rodionov, V. Ryabov, and K. Shpakov, Anisotropy in hard bremsstrahlung from a high-voltage laboratory simulation of an atmospheric discharge, *Plasma Sources Sci. Technol.* **28**, 095014 (2019).
- [32] F. B. Gross, *Frontiers in Antennas: Next Generation Design & Engineering* (McGraw-Hill, New York, 2011).

- [33] C. A. Balanis, *Antenna Theory: Analysis and Design* (John Wiley & Sons, New York, 2015).
- [34] R. J. Thomas, P. R. Krehbiel, W. Rison, S. J. Hunyady, W. P. Winn, T. Hamlin, and J. Harlin, Accuracy of the lightning mapping array, *J. Geophys. Res.: Atmos.* **109**, 2004JD004549 (2004).
- [35] A. Englesbe, J. Elle, R. Schwartz, T. Garrett, D. Woodbury, D. Jang, K.-Y. Kim, H. Milchberg, R. Reid, A. Lucero *et al.*, Ultrabroadband microwave radiation from near- and mid-infrared laser-produced plasmas in air, *Phys. Rev. A* **104**, 013107 (2021).
- [36] P. Kochkin, Understanding lightning: Experiments on meter long discharges and their x-rays, *Ph.D. dissertation, Technische Universiteit Eindhoven*, 2014.
- [37] S. Vayanganie, V. Cooray, M. Rahman, P. Hettiarachchi, O. Diaz, and M. Fernando, On the occurrence of ‘bead lightning’ phenomena in long laboratory sparks, *Phys. Lett. A* **380**, 816 (2016).
- [38] S. Nijdam, J. Teunissen, and U. Ebert, The physics of streamer discharge phenomena, *Plasma Sources Sci. Technol.* **29**, 103001 (2020).
- [39] E. Bazelyan and N. Popov, Stepwise development of a positive long spark in the air, *Plasma Phys. Rep.* **46**, 293 (2020).
- [40] S. Huang, W. Chen, Z. Fu, Y. Fu, N. Xiang, X. Qiu, W. Shi, D. Cheng, and Z. Zhang, Separate luminous structures leading positive leader steps, *Nat. Commun.* **13**, 3655 (2022).
- [41] Y. Fu, W. Chen, Y. Zhao, L. Ding, Z. Fu, N. Xiang, X. Qiu, J. Gu, Z. Pei, Z. Zhang *et al.*, Observations of the breakthrough phase of attachment process in laboratory long sparks, *Geophys. Res. Lett.* **49**, e2022GL099193 (2022).
- [42] S. Huang, W. Chen, Z. Fu, N. Xiang, Y. Ding, D. Cheng, J. Gu, and Z. Pei, On the step type of continuous propagating positive leader in laboratory-scale long spark discharges, *Geophys. Res. Lett.* **49**, e2022GL097890 (2022).
- [43] J. Hill, M. Uman, and D. Jordan, High-speed video observations of a lightning stepped leader, *J. Geophys. Res.: Atmos.* **116**, 2011JD015818 (2011).
- [44] M. M. Saba, C. Schumann, T. A. Warner, M. A. S. Ferro, A. R. de Paiva, J. Helsdon, Jr., and R. E. Orville, Upward lightning flashes characteristics from high-speed videos, *J. Geophys. Res.: Atmos.* **121**, 8493 (2016).
- [45] Y. Liu, X. Wang, X. Liu, L. Liu, G. Liu, M. Liao, L. Qu, B. Luo, H. Cai, J. He *et al.*, Branching morphology of negative leaders with different propagation directions in natural lightning, *Atmosphere* **13**, 1217 (2022).
- [46] M. M. Saba, D. R. R. da Silva, J. G. Pantuso, and C. L. da Silva, Close view of the lightning attachment process unveils the streamer zone fine structure, *Geophys. Res. Lett.* **49**, e2022GL101482 (2022).
- [47] P. Wilson, A. Ondrejka, M. Ma, and J. Ladbury, *Electromagnetic Fields Radiated from Electrostatic Discharges: Theory and Experiment* (National Institute of Standards and Technology, Gaithersburg, MD, 1988).
- [48] B. M. Bolotovskiy and A. V. Serov, Moving finite-size dipole emission, *Bull. Lebedev Phys. Inst.* **34**, 73 (2007).
- [49] L. Guo, H.-W. Zhang, and H.-C. Wu, High-frequency radio-wave emission by coherent transition radiation of runaway electrons produced by lightning stepped leaders, *Phys. Plasmas* **29**, 093102 (2022).
- [50] V. Cooray, G. Cooray, M. Rubinstein, and F. Rachidi, Ionization waves enhance the production of x-rays during streamer collisions, *Atmosphere* **12**, 1101 (2021).
- [51] N. Petrov, Synchrotron mechanism of x-ray and gamma-ray emissions in lightning and spark discharges, *Sci. Rep.* **11**, 19824 (2021).
- [52] P. Kapitza, High power electronics, *Sov. Phys. Usp.* **5**, 777 (1963).
- [53] S. A. Kaplan and V. N. Tsytovich, Plasma radiation mechanisms in astrophysics, *Sov. Phys. Usp.* **12**, 42 (1969).
- [54] D. Melrose, Collective plasma radiation processes, *Annu. Rev. Astron. Astrophys.* **29**, 31 (1991).
- [55] M. V. Kuzelez and A. A. Rukhadze, Waves in inhomogeneous plasmas and liquid and gas flows. Analogies between electro- and gas-dynamic phenomena, *Phys. Usp.* **61**, 748 (2018).
- [56] X. Shao and P. Krehbiel, The spatial and temporal development of intracloud lightning, *J. Geophys. Res.: Atmos.* **101**, 26641 (1996).
- [57] W. Winn, G. Aulich, S. Hunyady, K. Eack, H. Edens, P. Krehbiel, W. Rison, and R. Sonnenfeld, Lightning leader stepping, K changes, and other observations near an intracloud flash, *J. Geophys. Res.: Atmos.* **116**, 2011JD015998 (2011).
- [58] Z. Han, Z. Chun, G. Shanqiang, F. Wanxing, W. Haitao, L. Enze, G. Juntian, and T. Hantao, Lightning imaging with thunder using broadband direction-of-arrival estimation technique, in *2016 33rd International Conference on Lightning Protection (ICLP)* (IEEE, New York, 2016), pp. 1–7.
- [59] R. J. Blakeslee, T. J. Lang, W. J. Koshak, D. Buechler, P. Gatlin, D. M. Mach, G. T. Stano, K. S. Virts, T. D. Walker, D. J. Cecil *et al.*, Three years of the lightning imaging sensor onboard the International Space Station: Expanded global coverage and enhanced applications, *J. Geophys. Res.: Atmos.* **125**, e2020JD032918 (2020).
- [60] J. Johnson, R. Arechiga, R. Thomas, H. Edens, J. Anderson, and R. Johnson, Imaging thunder, *Geophys. Res. Lett.* **38**, 2011GL049162 (2011).
- [61] T.-K. Hong, S. Park, D. Chung, and B. Kim, Inversion of acoustic thunder source spectral model from thunder-induced seismic waves in megacity, *Geophys. J. Int.* **233**, 107 (2022).
- [62] O. Scholten, B. M. Hare, J. Dwyer, N. Liu, C. Sterpka, S. Buitink, T. Huege, A. Nelles, and S. ter Veen, Time resolved 3D interferometric imaging of a section of a negative leader with LOFAR, *Phys. Rev. D* **104**, 063022 (2021).
- [63] B. Hare, O. Scholten, A. Bonardi, S. Buitink, A. Corstanje, U. Ebert, H. Falcke, J. Hörandel, H. Leijnse, P. Mitra *et al.*, LOFAR lightning imaging: Mapping lightning with nanosecond precision, *J. Geophys. Res.: Atmos.* **123**, 2861 (2018).
- [64] N. Liu, O. Scholten, J. R. Dwyer, B. M. Hare, C. F. Sterpka, J. N. Tilles, and F. D. Lind, Implications of multiple corona bursts in lightning processes for radio frequency interferometer observations, *Geophys. Res. Lett.* **49**, e2021GL097367 (2022).
- [65] C. Sterpka, J. Dwyer, N. Liu, B. Hare, O. Scholten, S. Buitink, S. t. Veen, and A. Nelles, The spontaneous nature of lightning initiation revealed, *Geophys. Res. Lett.* **48**, e2021GL095511 (2021).
- [66] C. Sterpka, J. Dwyer, N. Liu, N. Demers, B. Hare, O. Scholten, and S. ter Veen, Ultra-slow discharges that precede lightning initiation, *Geophys. Res. Lett.* **49**, e2022GL101597 (2022).

- [67] N. Y. Liu, O. Scholten, B. M. Hare, J. R. Dwyer, C. F. Sterpka, I. Kolmašová, and O. Santolík, LOFAR observations of lightning initial breakdown pulses, *Geophys. Res. Lett.* **49**, e2022GL098073 (2022).
- [68] B. M. Hare, O. Scholten, S. Buitink, J. R. Dwyer, N. Liu, C. Sterpka, and S. ter Veen, Characteristics of recoil leaders as observed by LOFAR, *Phys. Rev. D* **107**, 023025 (2023).